Dynamics and Instabilities of Vortex Pairs

Thomas Leweke,[1] Stéphane Le Dizès,[1] and Charles H.K. Williamson[2]

[1]IRPHE, UMR 7342, CNRS, Aix-Marseille Université, Centrale Marseille, 13384 Marseille, France; email: leweke@irphe.univ-mrs.fr

[2]Sibley School of Mechanical and Aerospace Engineering, Cornell University, Ithaca, New York 14850

Annu. Rev. Fluid Mech. 2016. 48:507–41

The *Annual Review of Fluid Mechanics* is online at fluid.annualreviews.org

This article's doi: 10.1146/annurev-fluid-122414-034558

Keywords

vortex interactions, merging, Crow instability, elliptic instability, ground effect

Abstract

This article reviews the characteristics and behavior of counter-rotating and corotating vortex pairs, which are seemingly simple flow configurations yet immensely rich in phenomena. Since the reviews in this journal by Widnall (1975) and Spalart (1998), who studied the fundamental structure and dynamics of vortices and airplane trailing vortices, respectively, there have been many analytical, computational, and experimental studies of vortex pair flows. We discuss two-dimensional dynamics, including the merging of same-sign vortices and the interaction with the mutually induced strain, as well as three-dimensional displacement and core instabilities resulting from this interaction. Flows subject to combined instabilities are also considered, in particular the impingement of opposite-sign vortices on a ground plane. We emphasize the physical mechanisms responsible for the flow phenomena and clearly present the key results that are useful to the reader for predicting the dynamics and instabilities of parallel vortices.

1. INTRODUCTION

Vortices are basic ingredients of transitional and turbulent flows, and studying their fundamental dynamics and interactions helps us understand the behavior of the often-complicated flows encountered in nature or industry. A pair of straight parallel vortices is one of the elementary vortex configurations considered in the literature, motivated to a large extent by its relevance to the problem of aircraft trailing wakes. Any horizontally flying vehicle generates a counter-rotating vortex pair in its far wake, which can represent a potential hazard for following vehicles, and corotating configurations are present in the near wake of aircraft wings with lowered flaps.

Despite their conceptual simplicity, vortex pairs exhibit a variety of complex behaviors, ranging from two-dimensional dynamics (rotation, merging) to three-dimensional instabilities. **Figure 1** shows an example in which the simultaneous growth of two distinct instabilities of a counter-rotating vortex pair is observed in a laboratory experiment, a numerical simulation, and a full-scale aircraft wake.

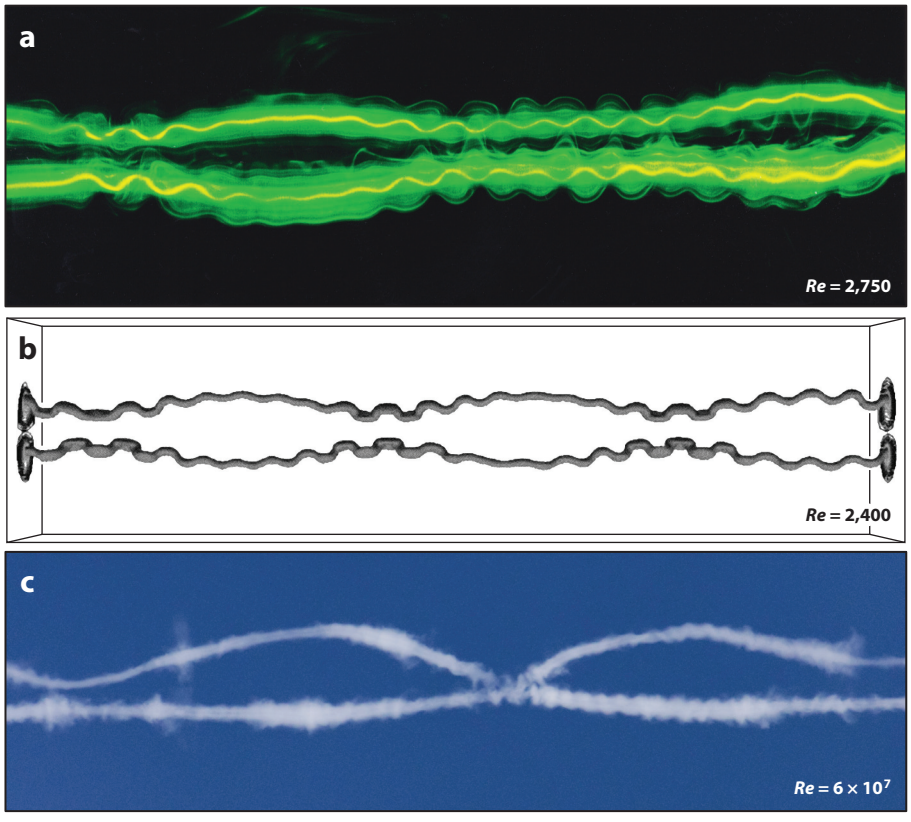

Figure 1

Visualizations of long-wave and shortwave instabilities developing in counter-rotating pairs of equal-strength vortices. (*a*) Dye visualization in a water tank at $Re = 2{,}750$. The field of view is approximately 14 cm × 42 cm. Panel *a* taken with permission from Leweke & Williamson (1998). (*b*) Numerical simulation with $Re = 2{,}400$. Panel *b* taken with permission from Laporte & Corjon (2000), copyright AIP Publishing LLC. (*c*) Photograph of the jet condensation trails from a Boeing 747 at $Re \approx 6 \times 10^7$. The field of view is approximately 150 m × 520 m. Panel *c* copyright 2011, Herbert Raab, reproduced with permission.

In the following, we review the dynamics and instabilities of vortex pairs in a homogeneous incompressible fluid. After recalling the properties of the two-dimensional base flows, which depend primarily on the circulation ratio of the two vortices, we focus on three major evolution mechanisms characterizing these flows: two-dimensional merging of corotating vortices, the three-dimensional Crow instability of counter-rotating vortices, and shortwave elliptic instability. The results concerning the structure and growth rate of these instabilities are then used to analyze the configuration of a vortex pair approaching a solid wall. We also address the interactions between the various phenomena.

Previous reviews including this topic were provided by Widnall (1975) and Saffman (1992). Much of the recent work related to aircraft trailing vortices is summarized in a special issue edited by Crouch & Jacquin (2005) and in Breitsamter (2011), following several earlier surveys (NATO 1996, Spalart 1998, Rossow 1999, Gerz et al. 2002).

2. TWO-DIMENSIONAL DYNAMICS

In this section, we consider two-dimensional dynamics of both counter-rotating and corotating vortices and discuss the most common vortex models to represent such vortex pairs. We analyze the strain field and elliptic flows within vortices and discuss the phenomenon of vortex merging.

2.1. Vortex Pair Models and Their Properties

As long as the vortices are far apart, their displacements can be described in the framework of point vortices by concentrating the circulation of each vortex in its center. The circulation and vortex center are defined by

$$\Gamma = \int_{\mathcal{D}} \omega \, \mathrm{d}S \quad \text{and} \quad \mathbf{X}^{\mathbf{c}} = \frac{1}{\Gamma} \int_{\mathcal{D}} \mathbf{X} \omega \, \mathrm{d}S, \tag{1}$$

where $\mathrm{d}S$ is a surface element at coordinate $\mathbf{X}$ of the planar domain $\mathcal{D}$ containing the vorticity ω of the vortex. A vortex Reynolds number can be defined as $Re = \Gamma/\nu$, where ν is the kinematic viscosity of the fluid. All possible arrangements for two point vortices, with circulations Γ_1 and Γ_2, preserve the distance (b) between them. This is a consequence of the conservation of linear or angular impulse. A symmetric counter-rotating pair ($\Gamma_1 = -\Gamma_2 = \Gamma$) translates with a constant straight-line speed $U = \Gamma/(2\pi b)$ (**Figure 2*a***). For all other counter- and corotating cases in **Figure 2**, for which $\Gamma_1 + \Gamma_2 \neq 0$, the vortices rotate around each other [i.e., around the invariant vorticity center $(\Gamma_1 \mathbf{X}_1^{\mathbf{c}} + \Gamma_2 \mathbf{X}_2^{\mathbf{c}})/(\Gamma_1 + \Gamma_2)$] at an angular velocity $\Omega = (\Gamma_1 + \Gamma_2)/(2\pi b^2)$.

As shown below, it is crucial to interpret the vorticity dynamics in the comoving frame when studying vortex pair flows. The streamlines for equal-strength vortices are shown in **Figure 3**. In the comoving reference frame, the counter-rotating pair comprises an inner and outer region, bounded by a separatrix streamline. The corotating pair exhibits a more complex structure, with an outer recirculation region, an inner core region, and a region between the two, referred to as the inner recirculation region, in which the fluid travels around both vortices. These regions are key to understanding vortex merging (see Section 2.3).

For each finite-size vortex, a characteristic radius a can be defined from the second-order moment of vorticity:

$$a^2 = \frac{1}{\Gamma} \int_{\mathcal{D}} |\mathbf{X} - \mathbf{X}^{\mathbf{c}}|^2 \omega \, \mathrm{d}S. \tag{2}$$

When this core size is small compared to the separation distance b, an asymptotic theory in the limit of small a/b can be used to describe the vortex core characteristics (Ting & Tung 1965). Each

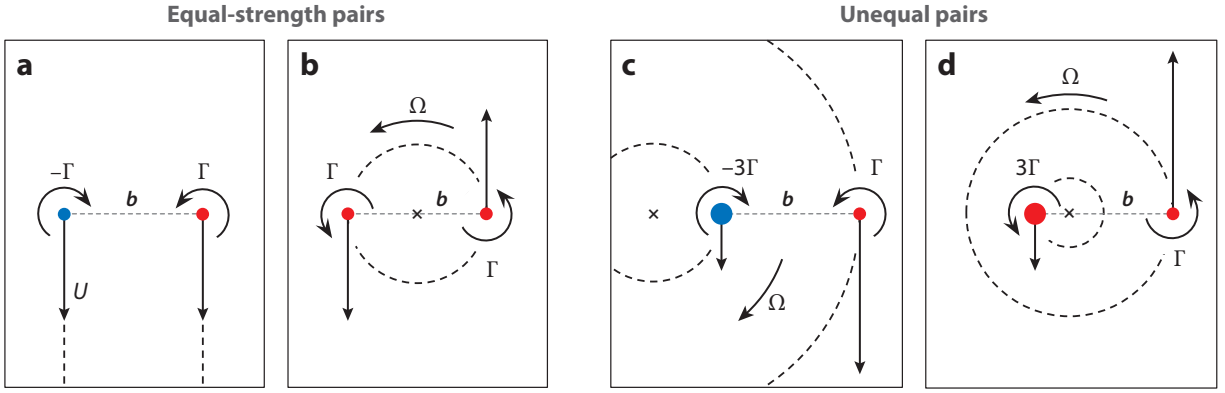

Figure 2

Trajectories of two-dimensional point vortex pairs, with separation distance b and circulation $\Gamma > 0$: (*a*,*b*) equal-strength counter- and corotating pairs and (*c*,*d*) unequal counter- and corotating pairs. The straight arrows represent the instantaneous velocity of each vortex, and the × in panels *b*–*d* marks the vorticity center of the pair.

vortex is then axisymmetric at leading order and is characterized by its radial profiles of vorticity and axial velocity, in the cylindrical reference frame (r, θ, z) centered on its $\mathbf{X}^c$ (see **Figure 4*a***). The axial flow component affects only the three-dimensional dynamics; we do not consider it further in this section.

Most studies have focused on the Rankine vortex model (a circular patch of uniform vorticity) for its analytical convenience or the Lamb-Oseen vortex model (Gaussian vorticity profile) for its

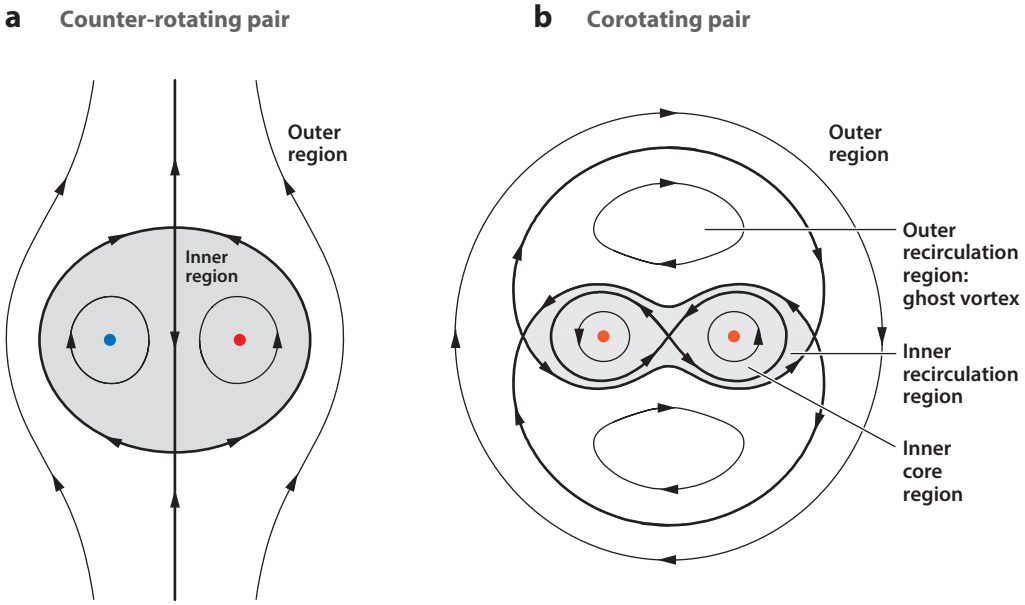

Figure 3

Streamline patterns of equal-strength point vortex pairs in the frame of reference moving with the vortices. (*a*) Counter-rotating pair in the translating frame. (*b*) Corotating pair in the rotating frame. Various regions can be identified, bounded by separatrices (*thick lines*) connected to hyperbolic points.

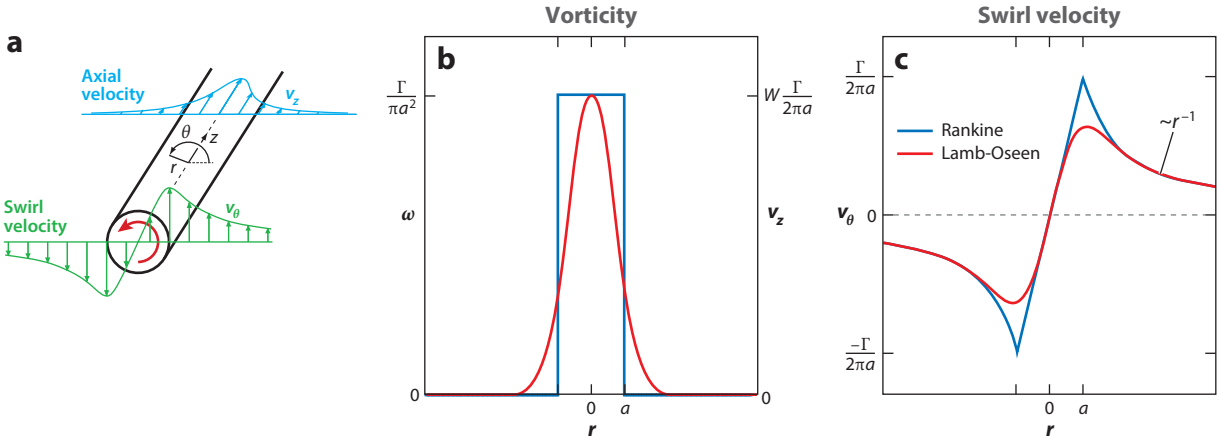

Figure 4

(*a*) Schematic illustration of vortex velocity profiles. (*b*) Vorticity ω and (*c*) swirl velocity v_θ for Rankine and Lamb-Oseen vortices. A possible additional velocity v_z in the direction of the vortex axis is assumed to be proportional to the vorticity. W is a nondimensional parameter representing the ratio between the maximum axial velocity and maximum swirl velocity.

good agreement with experimental data. The profiles of vorticity and azimuthal velocity of these models are as follows:

$$\text{Rankine vortex:} \quad \omega = \begin{cases} \Gamma/(\pi a^2) & r \le a \\ 0 & r > a \end{cases}, \quad v_\theta = \begin{cases} \Gamma r/(2\pi a^2) & r \le a \\ \Gamma/(2\pi r) & r > a \end{cases}, \tag{3}$$

$$\text{Lamb-Oseen vortex:} \quad \omega = \frac{\Gamma}{\pi a^2}\exp(-r^2/a^2), \quad v_\theta = \frac{\Gamma}{2\pi r}[1-\exp(-r^2/a^2)]. \tag{4}$$

These classic distributions are illustrated in **Figure 4**. For both cases, the characteristic core radius a is given by the relation in Equation 2. A list of other vortex models, used primarily to describe aircraft wake vortices, can be found in Gerz et al. (2002).

A first departure from axisymmetry, involving elliptic rather than circular streamlines, is associated with the strain field felt by each vortex (**Figure 5**). The combination of strain and rotation causes the elliptic streamlines to be oriented at 45° to the principal stretching axis. The vortex of circulation Γ_1 generates at the center of the second vortex, of circulation Γ_2, a strain field of

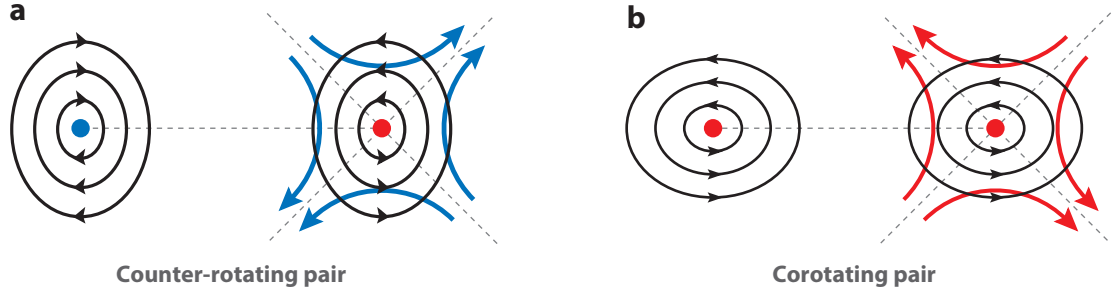

Figure 5

Schematic illustration of the elliptic streamlines resulting from the vortex core vorticity and strain (*colored arrows*) induced by the neighboring vortex for (*a*) counter-rotating and (*b*) corotating pairs.

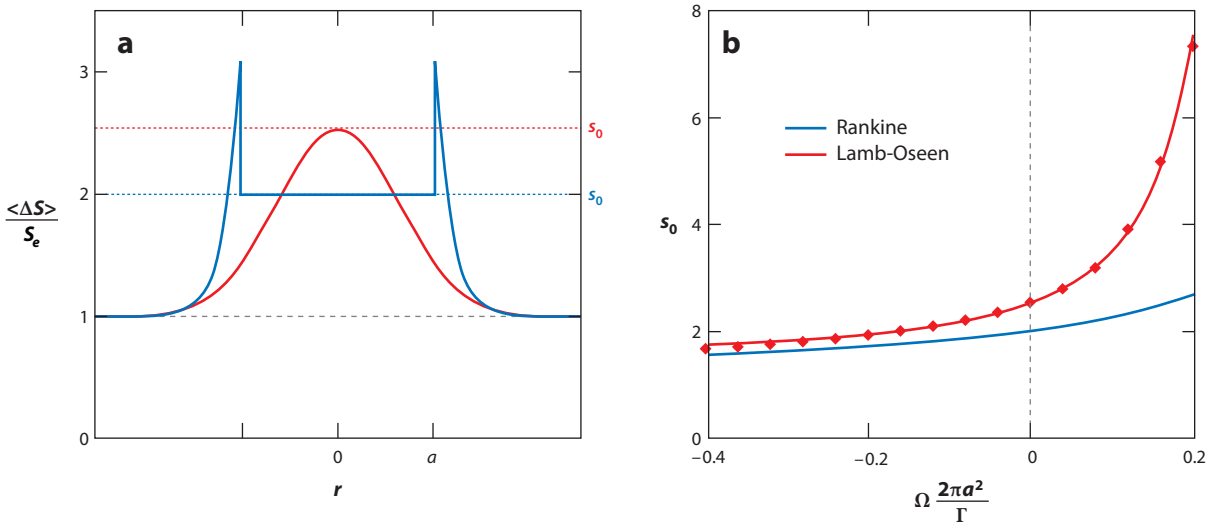

Figure 6

(*a*) Radial profiles of the (azimuthally averaged) strain increase ΔS for vortices placed in a weak, uniform, and stationary (nonrotating) external strain field of strength S_e. The jump at $r = a$ for the Rankine vortex is linked to the discontinuity of the vorticity at the core radius. (*b*) Maximum strain increase at the vortex center for external strain fields rotating at angular velocity Ω. For the Lamb-Oseen vortex, diamond symbols represent numerical results, and the red line represents Equation 5.

amplitude $S_e = \Gamma_1/(2\pi b^2)$. As shown by Sipp et al. (2000) and Le Dizès & Verga (2002), an equilibrium state of the vortex in this strain field is possible when a_2/b is sufficiently small. The interaction between vorticity and strain is, however, strongly nonlinear (Moffatt et al. 1994, Le Dizès 2000A). Interestingly, the strain field in the core is enhanced by this interaction (i.e., the strain rate S_i in the center of the vortex is larger than the strain rate S_e induced solely by the other vortex) (**Figure 6*a***). The external strain causes a deformation of the vortex. This deformation in itself further increases the strain within the vortex. The ratio $s_0 = S_i/S_e$ depends on the rescaled angular rotation $\overline{\Omega} = \Omega(2\pi a_2^2/\Gamma)$ of the vortex system. For the Rankine vortex, it is given by the exact relation $s_0 = 2(1 - \overline{\Omega})/(1 - 2\overline{\Omega})$. For the Lamb-Oseen vortex, it is well fitted by the expression

$$s_0(\overline{\Omega}) = 1.5 + 0.1323(0.32 - \overline{\Omega})^{-9/5}, \tag{5}$$

valid for $-0.4 < \overline{\Omega} < 0.2$ (Le Dizès & Laporte 2002). These relations are plotted in **Figure 6*b***. s_0 diverges for a finite value of $\overline{\Omega}$ (0.32 for the Lamb-Oseen vortex, 0.5 for the Rankine vortex). In this situation, strong additional nonlinear effects are expected.

2.2. Equilibrium Solutions

Equilibrium states of uniform-vorticity patches were studied by Moore & Saffman (1971) for a strained vortex and then by Saffman & Szeto (1980) for vortex pairs using contour dynamics methods (Pullin 1992). Families of uniform-vorticity patches have been discovered by different continuation techniques, providing stability characteristics and bifurcation diagrams (e.g., Dritschel 1985, 1995), and the extension of these results to nonuniform vorticity has been investigated (Ehrenstein & Rossi 1999, Meunier et al. 2002). The stability of the nonuniform Lamb-Chaplygin vortex pair has been addressed by Luzzatto-Fegiz & Williamson (2012), who found stability in the inviscid

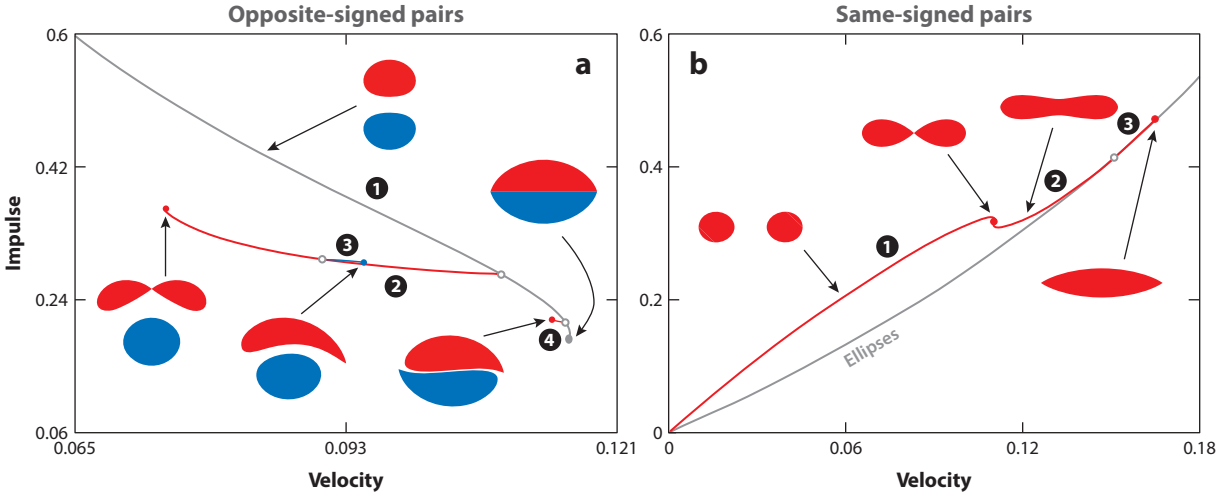

Figure 7

Imperfect velocity-impulse diagrams for equal-area pairs of uniform vortices: (*a*) opposite-signed pairs and (*b*) same-signed pairs. In both diagrams, line 1 represents stable solutions with distinct vortices, and line 2 represents unstable solutions. Panel *a* adapted with permission from Luzzatto-Fegiz & Williamson (2012) and panel *b* adapted with permission from Cerretelli & Williamson (2003a) and Luzzatto-Fegiz & Williamson (2010).

case, whereas more recently Brion et al. (2014) found that the pair is apparently unstable in the presence of viscosity.

The stability of such equilibria was initially the subject of some debate. Saffman & Szeto (1980) proposed an argument linking a particular bifurcation diagram (involving energy and impulse) to stability properties. In a study of the equilibrium and stability of up to eight corotating vortices, Dritschel (1985) pointed out the need for a rigorous basis for such an approach and noted that this methodology would miss instabilities associated with hitherto-undiscovered bifurcations. Dritschel (1995) calculated equilibria for same-signed and opposite-signed pairs with equal and unequal areas and performed detailed linear stability analyses. He found that the stability argument of Saffman & Szeto (1980) failed to detect the instability boundary for a large subset of opposite-signed pairs.

Although the topic of bifurcation methods for vortex dynamics deserves a separate review, it is relevant to mention here that an approach implementing imperfect velocity-impulse (IVI) diagrams has recently been introduced to define families of equilibrium vortex solutions for counter-rotating and corotating vortex pairs (**Figure 7**) (Luzzatto-Fegiz & Williamson 2010, 2012). Information concerning stability is given by turning points in impulse. Imperfections are introduced as a means to discover otherwise-hidden bifurcation branches. The IVI diagram for counter-rotating vortex pairs in **Figure 7*a*** is obtained by starting with stable solutions for the classical symmetric pair (shown by line 1). Introducing a small imperfection in the calculations enables the discovery of a new branch of solutions (branch 2), which is unstable. Surprisingly, despite their shape, these vortices translate along a straight line. Repeated use of imperfections also uncovers vortices without symmetry (branch 3) and antisymmetric equilibria (branch 4). Same-signed pairs are shown in **Figure 7*b*** (Cerretelli & Williamson 2003a, Luzzatto-Fegiz & Williamson 2010). The family involving two distinct stable vortices is labeled 1; these continue into a series of singly connected, unstable, dumbbell-shaped vortices (labeled 2), which are quite representative of vorticity distributions just prior to merging.

IVI diagram: imperfect velocity-impulse diagram

2.3. Merging of Corotating Vortices

Two identical vortices ultimately merge in viscous flow. A body of work has addressed the question of a critical core size above which merging takes place. Much early work comes from the computation of uniform-vorticity patches (Roberts & Christiansen 1972; Saffman & Szeto 1980; Overman & Zabusky 1982; Dritschel 1985, 1986) and from experiment (e.g., Hopfinger & van Heijst 1993). All of the above studies measured the normalized critical core size for the onset of merging to be $a/b = 0.29$–0.32. Meunier et al. (2002) deduced a criterion based on the core size as defined in Equation 2, which works well for vortices with a range of different vorticity distributions, with a critical size of typically $a/b \approx 0.24$.

The question of whether merging could be a consequence of an instability is still under debate. It has been associated with a change of the stability of vortex patches by Overman & Zabusky (1982) and Dritschel (1985), who found that vortices do not need to touch to become unstable; instability sets in when the gap between vortices decreases below 6% of the two-vortex length. This is consistent with the IVI diagram of **Figure 7*b***, in which instability occurs immediately before the red dot between branches 1 and 2 (actually at the maximum in impulse, before the two vortices touch). Intriguingly, the first mode to become unstable is antisymmetric and corresponds to what is found in experiment.

In the past few years, there has been a renewed focus on the physical mechanism of merging. The first step in understanding merging keys on the work of Dritschel (1985), who considered the corotating reference frame for same-sign vortices (**Figure 3*b***). This reference frame was also used by Melander et al. (1987, 1988), who observed in their computations that the diffusing vorticity could spill over from the inner core and inner recirculation region into the outer recirculation region, in which the velocity field of this so-called ghost vortex stretches the vorticity out into filaments. They viewed merging as an equivalent mechanism to what they proposed for a single elliptical vortex; namely, the vortex aspect ratio is reduced by an inviscid axisymmetrization process. In essence, the tilting of the corotating streamline pattern, relative to the vorticity contour pattern, gives rise to a reduction in the length of the ellipse. Melander et al. (1988) identified two stages during merging: the viscous metastable stage, governed by the dissipation timescale, and the convective merger stage, in which viscous effects are minimal and the vortices move toward each other rapidly. Meunier & Leweke (2001) and Meunier et al. (2002) defined a third stage: the final diffusion of the merged vortex. Cerretelli & Williamson (2003b) added a fourth stage (second diffusive stage), described below.

Figure 8 illustrates the stages of merger by the evolution of the vortex pair separation b. In the first diffusive stage, this distance is reasonably constant, as the vortex core grows according to the viscous diffusion law $a^2 = a_0^2 + 4\nu t$ (Meunier & Leweke 2001, Le Dizès & Verga 2002). When the vortex cores reach their critical size, the convective stage follows (see the central column of images in **Figure 9**), in which vortex separation rapidly reduces. Meunier et al. (2005) explained that, because some of the vorticity is advected to the outer region, thus increasing angular momentum, the vortex cores are forced together to conserve the total momentum. At the end of the convective phase, there is a second diffusive stage, in which the separation diminishes very slowly from Biot-Savart induction. The final merging of the two vorticity peaks is essentially achieved by diffusion of the vortices into each other, resulting in a single peak. One then reaches the merged diffusive stage, in which the vortex gradually becomes more axisymmetric. At sufficiently high Reynolds numbers, the vortex is surrounded by fine concentric filaments (right column in **Figure 9**). Josserand & Rossi (2007) studied the different merging phases over a wide range of Reynolds numbers and deduced that various parts of the flow field contribute to the rapid approach during

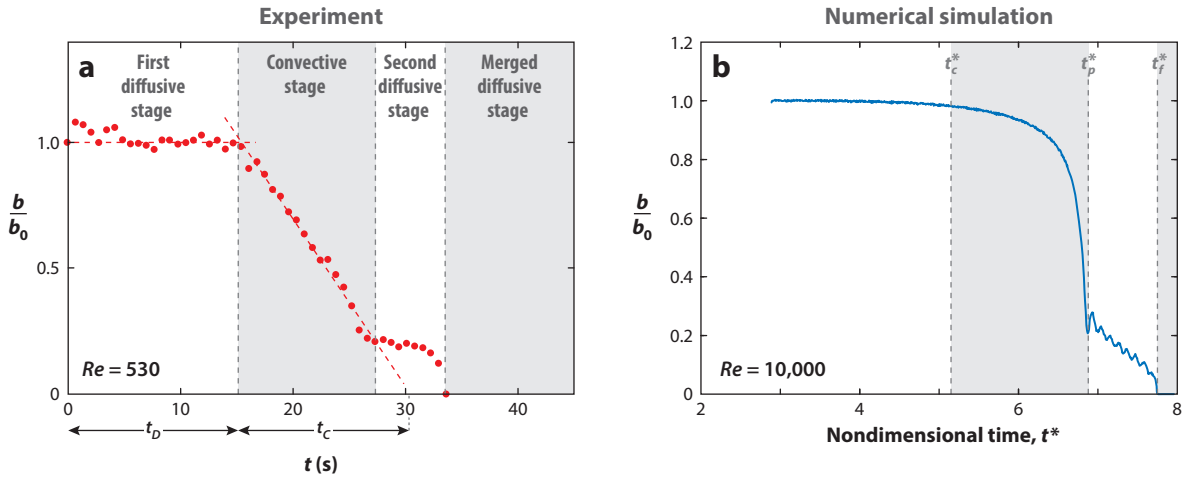

Figure 8

Evolution of the normalized vortex separation (b/b_0) with time during symmetric merging. (*a*) Experiment at $Re = 530$. Panel *a* adapted with permission from Cerretelli & Williamson (2003b). (*b*) Direct numerical simulation at $Re = 10{,}000$. Panel *b* adapted with permission from Josserand & Rossi (2007), copyright Elsevier Masson SAS. From these curves, it is possible to distinguish four distinct stages in the merging process.

the convective stage of merging. They found that approximately 30% of the total circulation orbits the central merged vortex during the final stage.

Why do the vortices get rapidly pushed together and merge? One could attempt to answer this question by superposing the vorticity onto its own streamline pattern in the corotating reference frame (**Figure 9*c***). The first image shows vorticity diffusing across the separatrices, from the core into the inner recirculation region, also called the exchange band, while some of the vorticity seeps into the outer recirculation region. In the middle image of **Figure 9*c***, anticlockwise vorticity is naturally concentrated by the velocity field upward and to the left of the left-hand vortex core, as well as downward and to the right of the right-hand vortex core. By Biot-Savart induction, one can immediately see that the core of the left-hand vortex is in proximity to a region of anticlockwise vorticity above it. The net result is that this vortex will move toward the other vortex; essentially both vortices rapidly move toward each other. There has been some debate, in a number of papers, as to whether the filaments are responsible for the merger (e.g., Velasco Fuentes 2005; Brandt & Nomura 2007, 2010; Josserand & Rossi 2007). One issue with such discussion is that the answer depends on the definition of the term filament, which could, for example, be taken to mean the tip all the way to the root (right next to the vortex cores) or could be just the thin filament within the outer region.

Rather than debate this point, one can directly deduce the vorticity responsible for the merger by decomposing the total field ω into symmetric and antisymmetric components ω_S and ω_A (**Figure 10**) (Cerretelli & Williamson 2003b):

$$\omega(x, y) = [\omega(x, y) + \omega(x, -y)]/2 + [\omega(x, y) - \omega(x, -y)]/2 = \omega_S(x, y) + \omega_A(x, y), \qquad (6)$$

with the coordinates x and y as defined in **Figure 10*a***. The conditions for the symmetric vorticity follow $\omega_S(x, y) = \omega_S(-x, y) = \omega_S(x, -y)$; therefore, the symmetric vorticity does not contribute

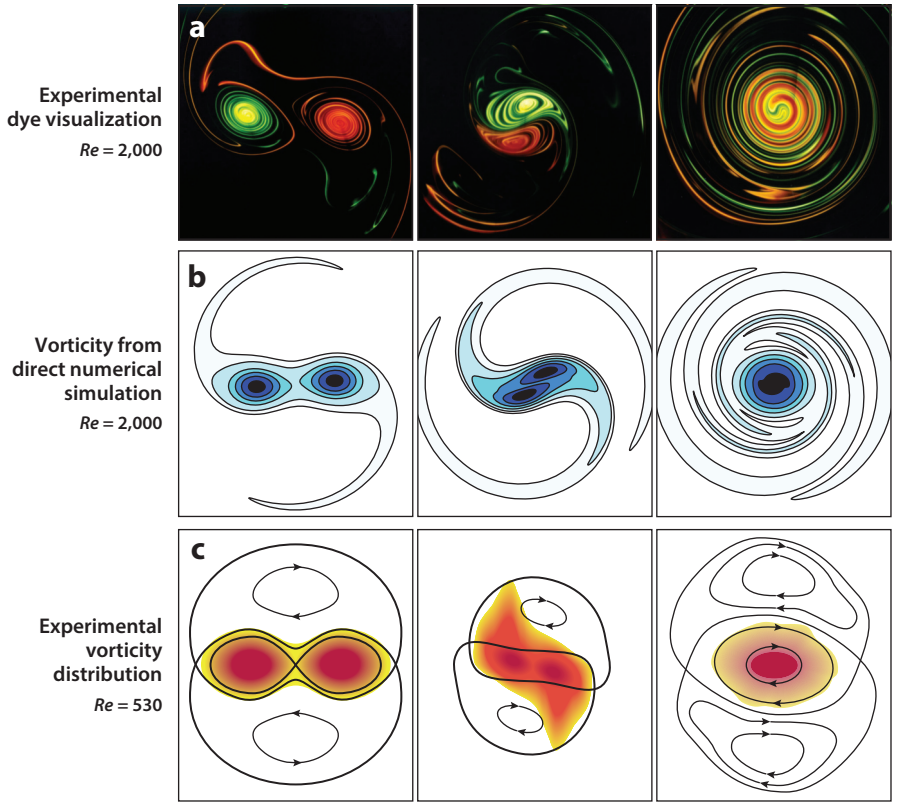

Figure 9

Merging of two equal laminar vortices. (*a*) Experimental dye visualization and (*b*) vorticity from a direct numerical simulation at $Re = 2{,}000$. Panels *a* and *b* reproduced with permission from Meunier et al. (2005), copyright Elsevier Masson SAS. (*c*) Experimental vorticity distribution and streamlines in the corotating frame at $Re = 530$. Panel *c* reproduced with permission from Cerretelli & Williamson (2003b).

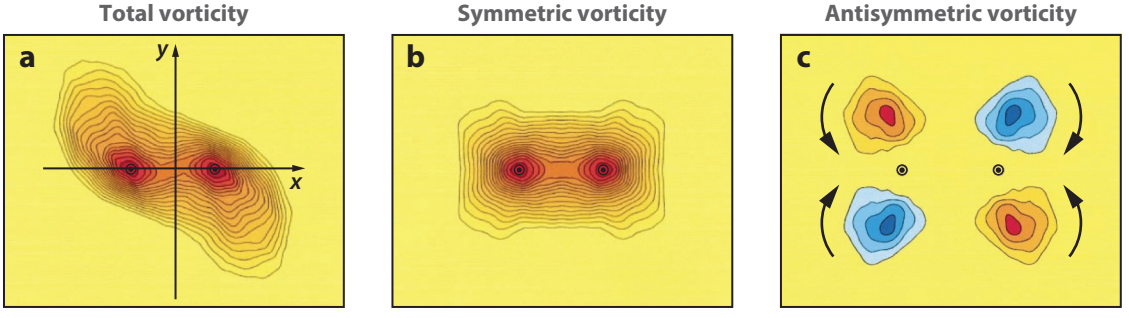

Figure 10

(*a*) Total vorticity field during the convective merging stage at $Re = 530$ and decomposition into (*b*) symmetric and (*c*) antisymmetric fields. Only the antisymmetric vorticity is responsible for merging. Figure adapted with permission from Cerretelli & Williamson (2003b).

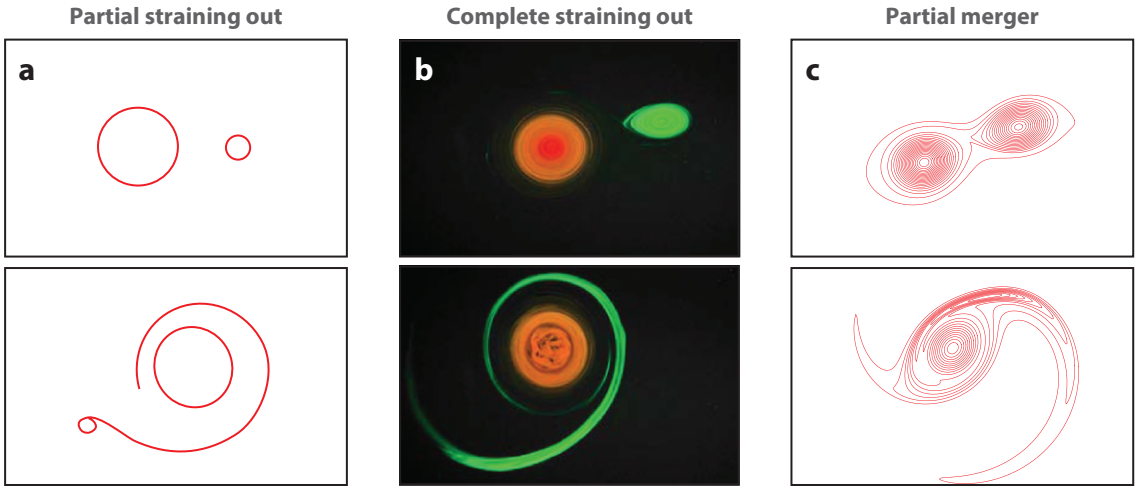

Figure 11

Various two-dimensional evolution scenarios for pairs of unequal, corotating vortices. (*a*) Partial straining out. Contour dynamics from Dritschel & Waugh (1992), reproduced with permission, copyright AIP Publishing LLC. (*b*) Complete straining out. Experiments from Trieling et al. (2005), reproduced with permission, copyright AIP Publishing LLC. (*c*) Partial merger. Numerical simulations from Brandt & Nomura (2010), reproduced with permission.

to the merging because the horizontal velocity anywhere along the x axis through the vorticity centroids is $u_S(x, 0) = 0$. This means that the entire velocity pushing the centroids together comes solely from the antisymmetric vorticity. The structure of the antisymmetric vorticity (**Figure 10*c***) comprises two counter-rotating vortex pairs, whose induced velocity readily pushes the vortex centroids together. Obviously, the picture will be influenced by the Reynolds number, but the approach does yield an understanding of why vortices merge.

Most studies have focused on the symmetric merger of two identical vortices, but corotating vortices could have a different size or different circulation. Phenomena such as partial straining out and partial merging (**Figure 11**) can be found in Dritschel & Waugh (1992), Yasuda & Flierl (1995), Brandt & Nomura (2010), and Jing et al. (2012). One vortex can be too weak to support the strain field generated by the other vortex. In this case, the weak vortex is stretched and destroyed by an elongation process that has been described, for instance, by Trieling et al. (1997). A continuous erosion process is also often active, in which part of the vorticity is stripped away (Legras & Dritschel 1993, Mariotti et al. 1994) when the hyperbolic stagnation point of the streamline pattern (see **Figure 3*b***) moves inside a vorticity region.

3. THREE-DIMENSIONAL INSTABILITIES

In this section, we review two mechanisms leading to three-dimensional instability in vortex pairs. The first involves perturbations displacing the vortices locally as a whole (i.e., without a change in their core structure), with wavelengths that are large compared to the core radius. For counter-rotating vortex pairs, these perturbations produce the long-wave Crow instability (Crow 1970). The second mechanism is linked to the amplification of shortwave perturbations inside the vortex cores. The growth of these modes results from the modification of the core structure by the external strain field induced by the neighboring vortex, as explained in the previous section. These effects produce the so-called elliptic instability (Kerswell 2002) in both counter- and corotating pairs.

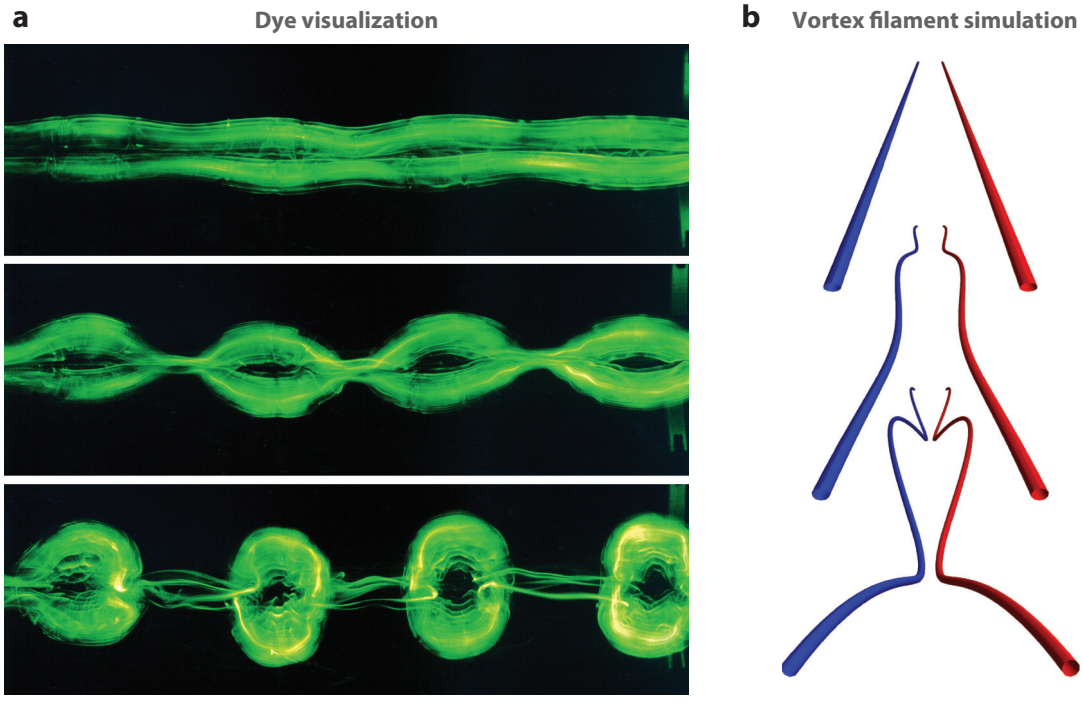

Figure 12

Long-wavelength Crow instability of a counter-rotating vortex pair. (*a*) Dye visualization in a water tank at $Re = 1{,}450$. The field of view is approximately 16 cm × 50 cm, and the vortices are moving toward the observer. Panel *a* reproduced with permission from Leweke & Williamson (2011), copyright AIP Publishing LLC. (*b*) Vortex filament simulations (inviscid) by Winckelmans et al. (2005), with the view along the center plane.

3.1. Crow Instability

A well-known feature observed in counter-rotating vortex pairs is a periodic long-wave deformation, which eventually leads to the decay of the pair. It can frequently be observed in the sky, behind aircraft flying at high altitude, when the wake vortices are visualized by condensation (**Figure 1*c***). Colloquially, these aircraft wakes are called contrails (condensation trails). Experiments and numerical simulations of this phenomenon (**Figure 12**) show that the sinusoidal deformations are symmetric with respect to the center plane of the pair and that they are inclined by approximately 45° to the line joining the two vortices (**Figure 13*a***). The deformation amplitude increases until the two vortex cores eventually touch and overlap at periodic locations. The subsequent vortex reconnection (Kida & Takaoka 1994) transforms the initial pair of line vortices into a series of three-dimensional vortex rings, which may persist for a certain time following their own oscillating dynamics (Dhanak & De Bernardinis 1981).

Vortex reconnection: breaking and rejoining of vortex lines

During the long-wave instability, the vortices are locally displaced as a whole, which is why this phenomenon can be described by a filament approach involving Biot-Savart induction. This was first carried out by Crow (1970) for the case of two counter-rotating Rankine vortices of equal strength. The analysis revealed the three main ingredients whose interaction leads to what is now called the Crow instability of counter-rotating vortex pairs. A given sinusoidal perturbation of the initially straight vortex is subject to the following mechanisms (**Figure 13*b***). First, there is its self-induced rotation, in the direction opposite the rotation of the core fluid, whose rate

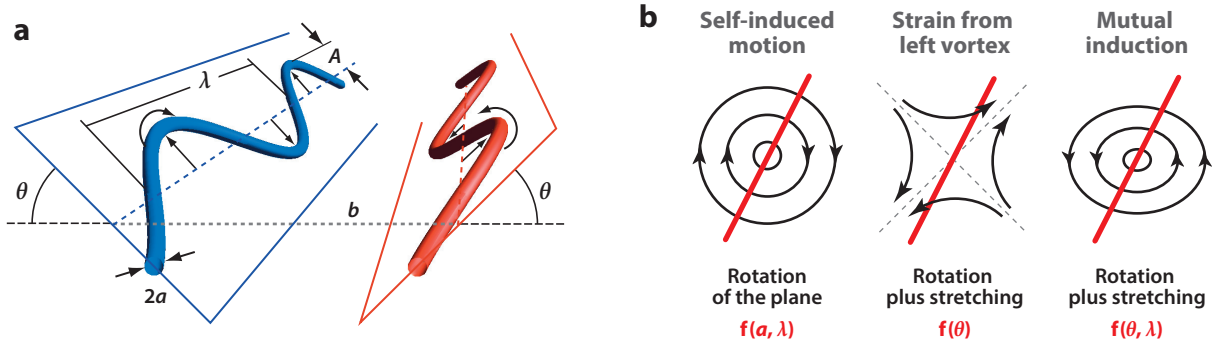

Figure 13

(*a*) Schematic illustration of the symmetric displacement mode associated with the Crow instability. (*b*) Illustration of the different mechanisms acting to rotate and stretch the plane containing the wavy perturbation (for the right vortex).

depends on the core size and the axial perturbation wavelength λ (Kelvin 1880). Second, there is the motion induced by the other vortex, assumed unperturbed, which, in the frame moving with the pair, consists of a plane stagnation point flow with maximum stretching in the 45° direction (**Figure 5*a***). Finally, there is the motion due to the combined perturbations of the two vortices. Similar to the previous effect, this motion induces a rotation and radial stretching on the perturbation plane (the plane containing the waviness), but it also depends on λ. Instability arises when, for a given combination (a, λ, θ), the three rotation effects cancel each other and the wave is held at a constant angle θ for which the total radial stretching rate is positive.

Widnall et al. (1971) extended the stability analysis toward more general vortex velocity profiles, also including an axial component, by introducing the concept of an equivalent Rankine vortex having the same self-induced dynamics for long wavelengths ($\lambda \gtrsim 16a$). The equivalent core size a_e, to be used in Crow's approach, can be calculated from the velocity profiles. For the case of a Batchelor vortex of radius a (Equation 4) and axial flow parameter W (**Figure 4*b***), one finds

$$a_e = a\sqrt{2}\exp\left[\frac{1}{4} - \frac{\gamma}{2} + \frac{W^2}{2}\right] \approx 1.36\,a\,\exp\left(\frac{W^2}{2}\right), \tag{7}$$

where $\gamma \approx 0.577$ is Euler's constant.

If the circulations of the two vortices are not equal and opposite, the rotation of the vortex pair needs to be taken into account in the analysis. For the perturbation plane to remain aligned with the strain field rotating at the same angular velocity Ω as the pair, the various rotation effects now have to add up to a rotation with Ω. For a pair of equal corotating vortices, Jiménez (1975) showed that this condition can never be achieved. Subsequently, in the framework of the filament approximation, Klein et al. (1995) and Fabre (2002) demonstrated that all corotating vortex pairs are stable, while all counter-rotating pairs are unstable, with respect to the Crow mechanism.

Following Fabre (2002), the growth rate σ of a wavy Crow-type perturbation with wavelength λ (wave number $k = 2\pi/\lambda$) of a pair of counter-rotating vortices having circulations $\Gamma_1 > 0$ and $|\Gamma_2| < \Gamma_1$, equivalent core radii a_1 and a_2, and a separation distance b is given by

$$\sigma = \frac{\Gamma_1}{2\pi b^2}\Re(E_{\max}), \tag{8}$$

where E_{max} is the eigenvalue with the largest real part of the matrix

$$\mathbf{L} = \begin{bmatrix} \eta_1 & 1+\varpi_1 & 0 & \Lambda\psi \\ -1-2\Lambda-\varpi_1 & \eta_1 & \Lambda\chi & 0 \\ 0 & \psi & \eta_2 & \Lambda(1+\varpi_2) \\ \chi & 0 & -2-\Lambda(1+\varpi_2) & \eta_2 \end{bmatrix}, \tag{9}$$

with $\Lambda = \Gamma_2/\Gamma_1$. The self-induction ($\varpi$), mutual-induction ($\psi$, χ), and viscous damping (η) functions are given by

Erratum >

$$\varpi_i = \frac{(kb)^2}{2+0.955ka_i+0.438(ka_i)^2}\left[\ln\left(\frac{2+2.151ka_i}{ka_i}\right)+\frac{1}{4}-\gamma\right], \tag{10}$$

$$\psi = (kb)^2 K_0(kb) + kbK_1(kb), \quad \chi = kbK_1(kb), \tag{11}$$

$$\eta_i = -(2\pi/Re)(a_i/b)^{-2}[1.54ka_i + (ka_i)^2]. \tag{12}$$

The K_j are modified Bessel functions of the second kind of order j, and the Reynolds number $Re = \Gamma_1/\nu$ here is based on the stronger vortex. ϖ and η are provided as numerical fits to the dispersion relation of the Crow perturbation mode, with η estimated based on results for the Lamb-Oseen vortex (without axial core flow).

From Equations 8–12, one can determine stability diagrams and growth rate curves. The examples in **Figure 14** for equal-strength vortices show the shortwave cutoff of the unstable domain. Because Equation 10 represents the exact self-rotation frequency, and not a long-wave approximation like the one used by Crow (1970), the spurious unstable wavelength band found in this initial study [and in Widnall's (1975) review] does not appear here. The agreement, in **Figure 14*b***, with a set of measurements from experiments such as those shown in **Figure 12*a*** is very good.

For vortices of equal strength, the most unstable wavelengths fall in a range between 6 and 10 times the separation distance b, depending on the relative core size a/b. For unequal vortices,

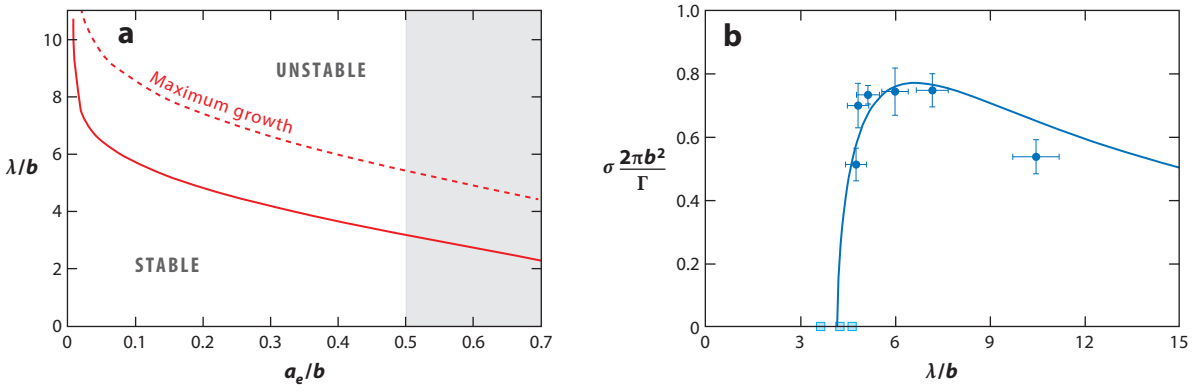

Figure 14

Crow instability for equal-strength counter-rotating vortices ($\Lambda = -1$). (*a*) Stability diagram for inviscid flow (the region with $a_e/b > 0.5$ has no physical relevance, as the cores are overlapping there). (*b*) Growth rate as a function of the normalized axial wavelength. The symbols represent experimental measurements in the range $1{,}500 < Re < 2{,}500$ (the instability could not be forced to take on the wavelengths marked by *square* symbols), and the line is the theoretical prediction (Equation 8) for $Re = 2{,}000$ and $a/b = 0.22$, which is representative for all experiments. Figure adapted with permission from Leweke & Williamson (2011), copyright AIP Publishing LLC.

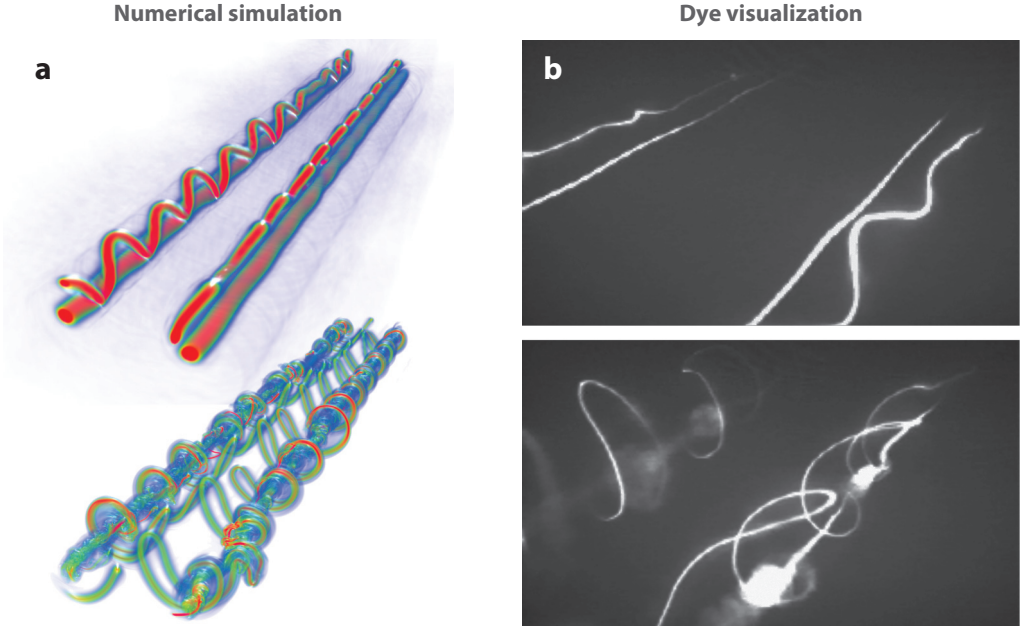

Figure 15

Crow instability of counter-rotating vortices of unequal strength with $\Lambda \approx -1/3$ (here as part of a four-vortex system), as found, for example, in the wake of a wing with flaps. (*a*) Numerical simulation. Panel *a* reproduced from Chatelain et al. (2008), with permission from Elsevier. (*b*) Dye visualization from towing-tank experiments. Panel *b* reproduced with permission from Ortega et al. (2003).

significantly smaller instability wavelengths, of the order of one spacing, can occur. One such case arises during the interaction of a vortex pair with a no-slip wall, as described in more detail in Section 5. Another configuration consists of four parallel line vortices, symmetrically arranged as two unequal counter-rotating pairs, each representing the vortex system behind an aircraft wing with outboard flaps. Although the four vortices evolve collectively, the initial dynamics are dominated by the asymmetric Crow instability of each pair. The numerical simulations by Chatelain et al. (2008) and experimental visualizations by Ortega et al. (2003) in **Figure 15** show how the perturbations of the weaker vortex develop into a series of Ω-loops, while the stronger vortex is much less affected by the instability.

Four-vortex systems, involving both corotating and counter-rotating pairs, have attracted some attention in the context of aircraft wake turbulence (Crouch et al. 2001, Fabre et al. 2002). The faster perturbation growth in the closely spaced pair behind each wing ($\sigma \sim b^{-2}$) may trigger and enhance the development of the Crow instability of the final primary vortex pair farther downstream and therefore accelerate the decay of the hazardous wake vortices.

3.2. Elliptic Instability

In addition to the long-wavelength Crow instability, vortex pairs develop shortwave perturbations inside the core of each vortex, with axial wavelengths scaling on the core radius. Clear visualizations of this phenomenon were obtained by Leweke & Williamson (1998) and Meunier & Leweke (2005) for counter- and corotating pairs, respectively. **Figure 16** shows the characteristic deformations associated with this instability, involving an invariant stream tube whose diameter is almost precisely half the axial wavelength. The vorticity field has a qualitatively similar structure,

Ω-loops: vortex loops shaped like the Greek letter Ω, resulting from a wavy filament in a strong external strain

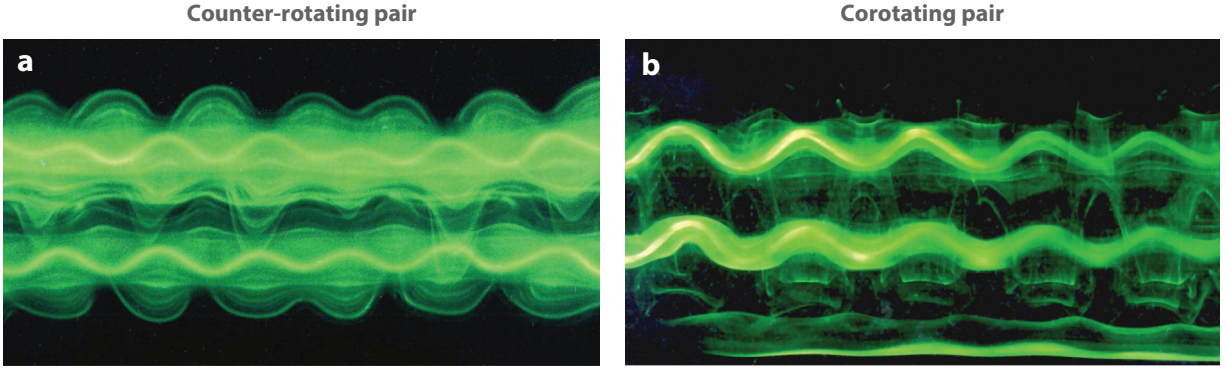

Figure 16

Water-tank dye visualizations of the elliptic instability: (*a*) counter-rotating vortex pair at $Re = 2{,}750$ (close-up of **Figure 1*a***) and (*b*) corotating vortex pair at $Re = 4{,}140$. Panel *a* reproduced with permission from Leweke & Williamson (1998) and panel *b* reproduced with permission from Meunier & Leweke (2001), copyright AIP Publishing LLC.

and these features can be used to help identify the elliptic instability in visualizations or numerical simulations.

The origin of this instability was first explained by Moore & Saffman (1975) and Tsai & Widnall (1976), following an analysis by Widnall et al. (1974) of the instability of a vortex ring. It results from a resonance mechanism between two perturbation waves (Kelvin modes) of the underlying axisymmetric structure of each vortex and the modification of this base flow induced by the strain from the other vortex. This resonance can lead to an exponential amplification of the involved Kelvin modes, causing the instability of the vortex. In the literature, it has been called the Moore-Saffman-Tsai-Widnall instability (e.g., Fukumoto 2003) or the Widnall instability (e.g., Sipp & Jacquin 2003). As discussed in Section 2 (**Figure 5**), an external strain produces flow with elliptical streamlines in the vortex core, which has been shown to be three-dimensionally unstable (see below). The shortwave instability is therefore now also referred to as elliptic instability. This phenomenon occurs in a variety of flow configurations (reviewed in Kerswell 2002).

The linear modes of a Rankine vortex were first determined by Kelvin (1880), whereas the linear modes of a Lamb-Oseen or Batchelor vortex were deduced by Le Dizès & Lacaze (2005) and Fabre et al. (2006). The velocity field of a Kelvin mode can be expressed as $\mathbf{u}_n(r) \cdot \exp[i(kz + m\theta - \omega t)]$. Here, k, m, and ω are the axial and azimuthal wave numbers and the (complex) frequency of the mode (not to be confused with the vorticity ω of Section 2) in the comoving reference frame of the vortex (**Figure 4*a***). The integer n characterizes the radial complexity of the mode; for a given azimuthal wave number m, it labels the branches of the dispersion relation $\omega(k)$. The elliptic perturbation induced by the strain of a neighboring vortex has azimuthal wave number $m = 2$; it is stationary ($\omega = 0$) in the comoving frame and uniform in the axial direction ($k = 0$). The condition of a triadic resonance of this perturbation with two Kelvin modes, $(k_1, m_1, \omega_1, n_1)$ and $(k_2, m_2, \omega_2, n_2)$, is therefore given by

$$k_1 = k_2, \quad |m_1 - m_2| = 2, \quad \omega_1 = \omega_2. \tag{13}$$

Kelvin mode: linear perturbation mode of an axisymmetric vortex, usually neutral or stable

For given m_1 and m_2, this condition is fulfilled for various combinations (n_1, n_2). It is, however, observed that elliptic instability is strongest when the two modes have a similar radial structure (i.e., $n_1 = n_2 = n$). In the following, the resulting instability modes will be referred to by the azimuthal wave numbers of the two contributing Kelvin modes and the label of their radial structure: (m_1, m_2, n).

Leweke & Williamson (1998) and Meunier & Leweke (2005) demonstrated that the core deformations observed experimentally in their vortex pairs without axial flow (**Figure 16**) correspond to a combination of two stationary helical waves, i.e., an instability mode $(m_1, m_2, n) = (-1, 1, 1)$, as initially suggested by Widnall et al. (1974) in the context of vortex rings. Tsai & Widnall (1976) calculated the growth rate of this mode for the case of a Rankine vortex. Eloy & Le Dizès (2001) and Fukumoto (2003) showed that numerous other unstable modes with similar growth rates exist in this type of vortex; none of them, however, was observed in experiments. This can be explained by the results obtained for the more realistic Lamb-Oseen vortex, for which only the stationary modes of the form $(-1, 1, n)$, the so-called bending modes, were found to have a significant growth rate (Eloy & Le Dizès 1999, Sipp & Jacquin 2003). For the other resonant configurations, the presence of a critical-layer singularity always dampens one of the involved Kelvin waves (Le Dizès 2004, Le Dizès & Lacaze 2005, Fabre et al. 2006). Only strongly deformed vortex pairs with large cores, such as the Lamb-Chaplygin dipole, were found to develop another subdominant instability mode of type $(2, 0, n)$ (Billant et al. 1999, Donnadieu et al. 2009).

Critical layer: fluid layer located at a radial distance where $\omega = mv_\theta/r + kv_z$ and where the inviscid perturbation with (k, m, ω) is singular

The generic character of the elliptic instability was demonstrated by Pierrehumbert (1986) and Bayly (1986), who analyzed the behavior of plane-wave solutions in an unbounded uniform elliptic flow. In the limit of small strain (S_i), Waleffe (1990) derived the now well-known expression for the maximum instability growth rate, $\sigma_{\max} = (9/16)S_i$, which was further generalized by Le Dizès (2000b) to account for arbitrary wave orientations and for rotation of the strain field. Applying these results locally at the vortex center, Le Dizès & Laporte (2002) provided a general expression[1] for the growth rate of the elliptic instability modes $(-1, 1, n)$ in a Lamb-Oseen vortex pair. They also included an estimate of the viscous damping, using the simple expression for plane waves given by Landman & Saffman (1987), but it was later shown that this overestimates the viscous damping rate (Roy et al. 2008, Donnadieu et al. 2009). An improved estimate can be made based on the numerically determined damping rate of the relevant Kelvin modes.

We here provide a corrected operational formula for the growth rate of the elliptic instability in a pair of Lamb-Oseen vortices with parameters $(\Gamma_1, \Gamma_2, a_1, a_2, b)$. The growth rate of the first two modes $(-1, 1, n)$, with $n = 1, 2$, in vortex 1 is given by

$$\sigma_1^{(n)} = \sqrt{\left(\frac{3}{4} - \frac{\overline{\Omega}_1}{4}\right)^4 s_0^2(\overline{\Omega}_1)\frac{\Gamma_2^2}{4\pi^2 b^4} - \left(\varpi^{(n)} - \overline{\Omega}_1\right)^2 \frac{\Gamma_1^2}{4\pi^2 a_1^4}} - \frac{\nu}{2\pi a_1^2}\zeta^{(n)}, \tag{14}$$

where $\overline{\Omega}_1 = (a_1/b)^2(\Gamma_1 + \Gamma_2)/\Gamma_1$, $s_0(\overline{\Omega}_1)$ is as defined in Equation 5, and

$$\varpi^{(1)} = -0.135(ka_1 - 2.26), \quad \zeta^{(1)} = 74.02 + 64.15(ka_1 - 2.26), \tag{15}$$

$$\varpi^{(2)} = -0.084(ka_1 - 3.95), \quad \zeta^{(2)} = 229.6 + 104.3(ka_1 - 3.95). \tag{16}$$

Equations 15 and 16 represent linear fits of the real and imaginary parts (frequency and damping rate, respectively) of the complex frequency of the first two Kelvin modes with azimuthal wave number $m = 1$, which can be written as $\omega \cdot (2\pi a^2/\Gamma) = \varpi^{(n)} - i\zeta^{(n)}/Re$, close to the resonant wave numbers $k_c^{(1)} = 2.26/a$ and $k_c^{(2)} = 3.95/a$. They provide good approximations of the numerically determined values in the interval $|k - k_c^{(n)}|a < 1$ and for $Re > 500$. In Equation 14, only the viscous damping term is different from Le Dizès & Laporte's formula. The growth rates of the instability in vortex 2 are obtained by exchanging the subscripts 1 and 2 in all expressions.

[1]There is a misprint in the main formula of Le Dizès & Laporte (2002, equation 6.1 and 6.2), where $(b/a_1)^2$ and $(b/a_2)^2$ should be replaced by $(b/a_1)^4$ and $(b/a_2)^4$, respectively.

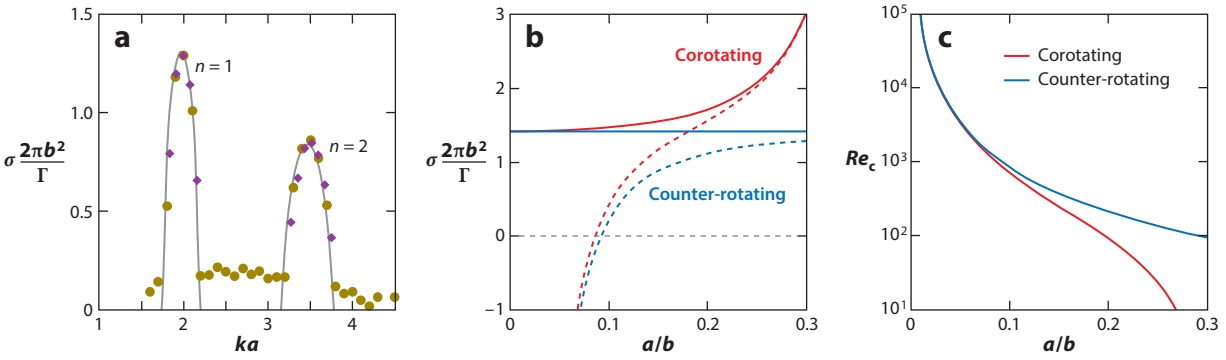

Figure 17

(*a*) Growth rate of the elliptic instability for a pair of identical corotating Gaussian vortices ($\Lambda = 1$) with $a/b = 0.14$ and $Re = 14{,}000$. Purple and dark yellow symbols represent data from numerical simulations using two different codes; the gray lines represent the theoretical prediction in Equation 14. Panel *a* adapted with permission from Roy et al. (2008), copyright AIP Publishing LLC. (*b*) Maximum growth rate [inviscid (*solid lines*) and $Re = 1{,}000$ (*dashed lines*)] and (*c*) critical Reynolds number for pairs of vortices with equal circulation.

Figure 17*a* compares the prediction of Equation 14 to results from direct numerical simulations of the instability in a pair of identical corotating Lamb-Oseen vortices. Other configurations have also been tested (Le Dizès & Laporte 2002, Donnadieu et al. 2009, So et al. 2011), each time showing the same good agreement. Equation 14 can then be used to explore the variation of the instability characteristics with the vortex pair parameters. **Figure 17*b*** plots the maximum growth rate for equal-strength pairs as a function of the rescaled core size a/b, for both inviscid and viscous ($Re = 1{,}000$) flow. Corotating vortices are found to be more unstable than counter-rotating vortices, and because their most unstable wavelength is larger, they are also less affected by viscosity. For a given ratio a/b, the vortex pair becomes unstable above a critical Reynolds number (**Figure 17*c***).

3.2.1. Effect of axial core flow. Axial flow may be present within the vortices. This is particularly the case for wing-tip vortices, which motivated Batchelor (1964) to develop his vortex model. Considering the effect of axial flow on the elliptic instability may therefore have some relevance for the problem of aircraft wake turbulence.

The axial velocity component does not modify the two-dimensional dynamics of the vortices, but it affects the three-dimensional elliptic instability, as it changes the characteristics of the vortex Kelvin waves. Lacaze et al. (2005) analyzed a Rankine vortex with a constant axial velocity in its core (see the right axis in **Figure 4*b***). They observed that the axial jet breaks the symmetry and that the resonance of the helical Kelvin modes with $m = \pm 1$ no longer leads to a stationary sinuous deformation. As for the case without axial flow, many other resonances are found, with growth rates close to the one for infinite elliptical flow, $(9/16)S_i$.

The case of the Batchelor vortex, i.e., a Lamb-Oseen vortex with a Gaussian axial velocity profile of amplitude $W\Gamma/(2\pi a)$ (**Figure 4*b***), was treated by Lacaze et al. (2007), who used the method of Moore & Saffman (1975) to systematically compute the growth rate associated with each vortex wave resonance. They showed that, as the axial flow amplitude increases, the stationary elliptic instability modes $(-1, 1, n)$ are stabilized and replaced by oscillatory modes involving different azimuthal wave numbers. The theoretical predictions were validated using direct numerical simulations of counter-rotating vortex pairs. Although many different modes are unstable, the

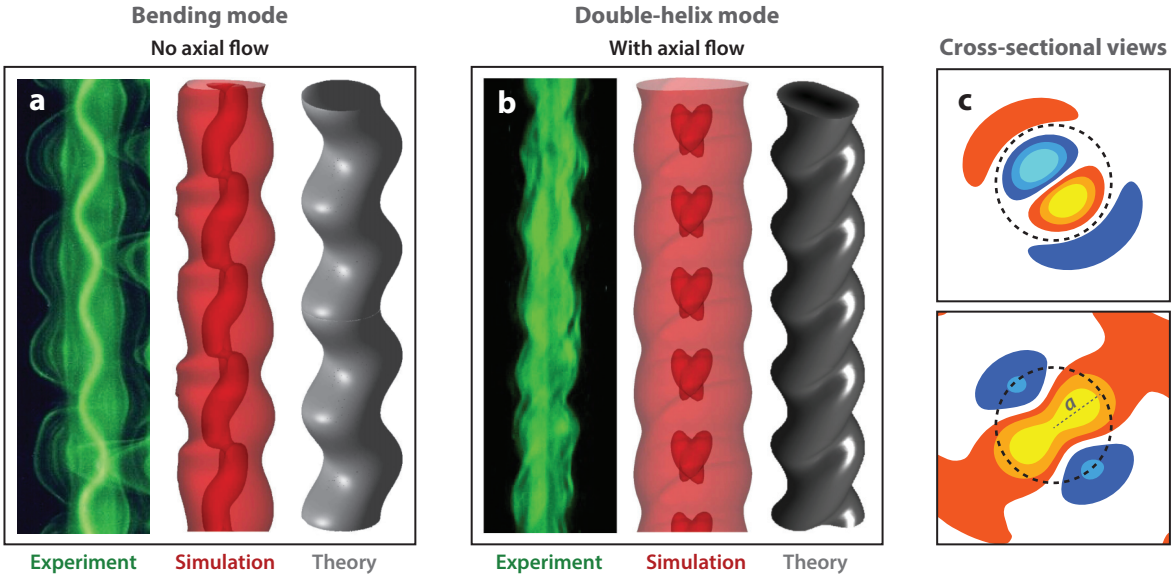

Figure 18

Elliptic instability modes. (*a*) Bending mode (−1, 1, 1) in a vortex without axial core flow and (*b*) double-helix mode (−2, 0, 1) in a vortex with axial flow. Experimental data reproduced with permission from Leweke & Williamson (1998) and Roy et al. (2011), and numerical simulation data reproduced with permission from Ryan & Sheard (2007). (*c*) Cross-sectional view of both modes, showing the axial perturbation vorticity. The dashed circle has radius a.

instability mode (−2, 0, 1), corresponding to the resonance of the first branches of the $m = -2$ and $m = 0$ Kelvin modes, plays a particularly important role, as it is the most unstable in a large domain of the k-W parameter space; it is expected to be the dominant instability mode for $0.3 < W < 0.65$ (see Lacaze et al. 2007). Numerical simulations (Ryan & Sheard 2007) and water channel experiments with wing-tip vortices (Roy et al. 2011) have provided clear evidence of the (−2, 0, 1) instability mode [see **Figure 18**, which also includes a direct comparison with mode (−1, 1, 1)]. For $W > 0.65$, the elliptic instability analysis is no longer relevant because each vortex is unstable with respect to the swirling jet instability (Mayer & Powell 1992), which has a much higher growth rate than does the elliptic instability.

Results obtained by direct numerical simulations of corotating Batchelor vortices of the same strength (Roy et al. 2008) or of different strengths (Ryan et al. 2012) show that the rotation of the vortex system does not fundamentally modify the stability characteristics. The modes observed for counter-rotating pairs are also present in corotating pairs, but as before, corotation tends to increase the growth rate and shift the unstable wave-number band to smaller values (Roy et al. 2008). We mention that various other instability modes, corresponding to resonances of Kelvin modes with possibly different labels n, can be observed in both corotating and counter-rotating systems, when either the Reynolds number or the relative core size a/b becomes large. Roy et al. (2008) showed that the instability bands of these modes tend to overlap as a/b increases, making the vortex system unstable to a wide spectrum of wavelengths.

3.2.2. Nonlinear evolution. The nonlinear evolution of the elliptic instability was previously discussed by Kerswell (2002). Although a weakly nonlinear evolution leading to a saturation of the

unstable mode is a priori possible (Waleffe 1989), Kerswell (1999) predicted that this mode could be destabilized by a secondary instability, again involving a triadic wave resonance mechanism, followed by other instabilities, possibly leading to a transition to turbulence. Eloy et al. (2003) observed this scenario for elliptical flow in a closed geometry, which also revealed more complicated breakdown and relaminarization processes that could be related to what was previously termed resonant collapse (see Kerswell 2002). For a strained vortex in an open configuration, Schaeffer & Le Dizès (2010) demonstrated numerically that a limit cycle for the elliptic mode (−1, 1, 1) could be obtained very close to the instability threshold Re_c (**Figure 17*c***). Far from this threshold, more complex dynamics are observed, involving the ejection of some of the vorticity away from the vortex core and the development of small scales rapidly dissipated by viscosity (Laporte & Corjon 2000, Schaeffer & Le Dizès 2010). After this turbulent regime, the vortex relaminarizes, and a new vortex with a larger core is formed, on which the elliptic instability can grow again (Laporte 2002, Schaeffer & Le Dizès 2010). This instability-breakdown-relaminarization process can repeat itself, leading to a rapid increase of the vortex core size on a convective timescale. This process could be the mechanism responsible for vortex core growth at very high Reynolds numbers, encountered, for example, in aeronautical applications (Laporte 2002).

The nonlinear evolution of the elliptic instability mode (−2, 0, 1) was analyzed by Ryan et al. (2012) for two counter-rotating, unequal-strength Batchelor vortices. They showed that the growth of this mode in the weaker vortex leads to the formation of secondary filamentary vortex structures, which are wrapped around the other vortex. It is not clear, however, if an instability-breakdown-relaminarization process also exists in the presence of axial flow.

The effect of a stable stratification on the mechanisms involved in the evolution of vortex pairs described in Sections 2 and 3 (i.e., merging and long- and shortwave instabilities) has been investigated by a number of authors. An overview of these studies is given in the sidebar, Vortex Pairs in a Stratified Fluid.

VORTEX PAIRS IN A STRATIFIED FLUID

Two main configurations can be determined in which the vortex axes are either parallel to the density gradient (vertical pairs) or perpendicular (horizontal pairs).

Vertical Pairs

Counter- and corotating vertical pairs in strong stratification exhibit a Crow-type zigzag instability, involving antisymmetric and symmetric displacements, respectively (Williamson & Chomaz 1997, Billant & Chomaz 2000, Otheguy et al. 2006). This is possible because the self-induced rotation of the wavy perturbations is in the same direction as the vortex core rotation (Billant 2010). The elliptic instability is weakened (Miyazaki & Fukumoto 1992) or even suppressed (Waite & Smolarkiewicz 2008) as the stratification is increased. The zigzag instability leads to a faster merging of corotating vortices (Otheguy et al. 2015).

Horizontal Pairs

Stratification was found to decrease the separation distance of descending counter-rotating pairs, which tends to enhance the development of the Crow and elliptic instabilities (Delisi & Robins 2000, Garten et al. 2001, Nomura et al. 2006). Interaction with baroclinic vorticity leads to a rapid decay of the pair (Holzäpfel et al. 2001). Merging of corotating vortices is delayed for low Reynolds numbers and accelerated for high Reynolds numbers (Brandt & Nomura 2007).

4. COMBINED EFFECTS

The previous sections treat each of the principal dynamical features observed in vortex pairs separately (i.e., two-dimensional merging and the three-dimensional Crow and elliptic instabilities). In a realistic pair, these phenomena can occur simultaneously, and the combination can produce a significantly different outcome than each mechanism acting alone. We here present two examples of such interactions, considering the effect of the elliptic instability on the merging of corotating vortices and on the development of the Crow instability of a counter-rotating pair.

4.1. Combined Merging and Elliptic Instability

Two parallel corotating vortices in three dimensions will merge in a uniform two-dimensional manner (**Figure 9**) for Reynolds numbers below the critical value Re_c for elliptic instability (**Figure 17*c***). When Re is increased above the threshold, not only does the elliptic perturbation become unstable, but the first diffusive stage also lasts longer, leaving more time for the instability to grow before the convective merging phase. When the nonlinear stage of the instability is reached, with breakdown into small scales and the ejection of vorticity away from the cores, a premature merging can be triggered for core sizes well below the two-dimensional critical size. This unstable merging was studied experimentally by Meunier & Leweke (2000, 2001, 2005) and numerically by Laporte (2002), Schaeffer & Le Dizès (2007), and Nybelen & Paoli (2009). These studies further showed that the final vortex after merging is turbulent and larger than that for the case of two-dimensional merging without instability. The visualizations in **Figure 19*a*** illustrate

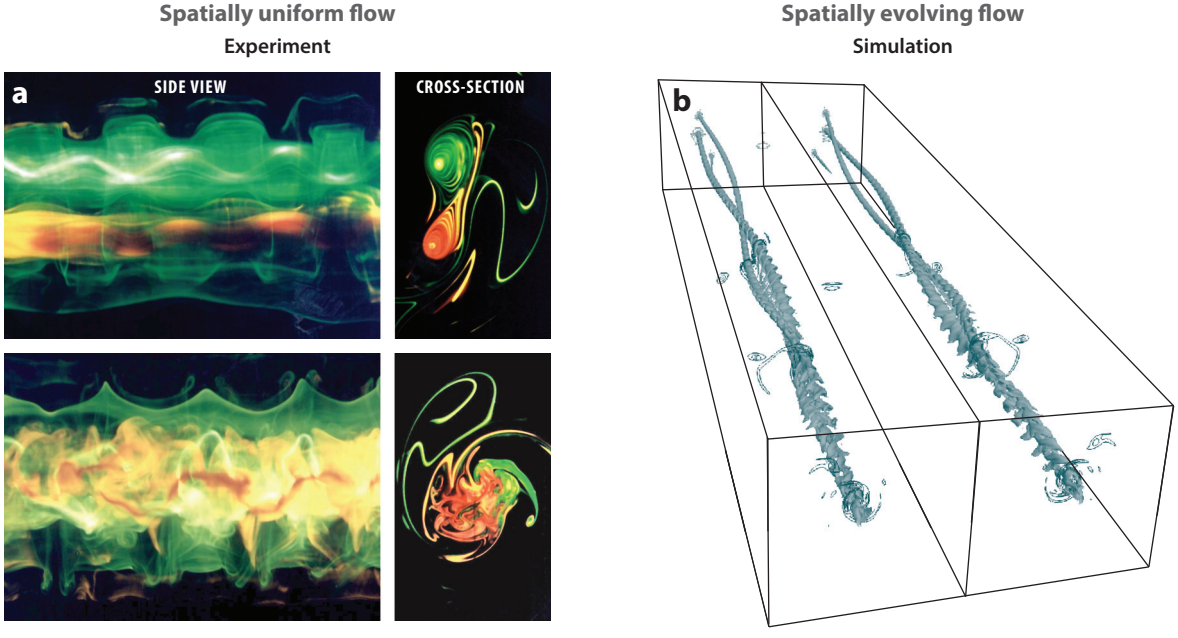

Figure 19

Unstable merging of corotating vortices. (*a*) Experimental dye visualization (side view and cross-sectional view at two times) at $Re = 4{,}000$. Panel *a* reproduced with permission from Meunier & Leweke (2005). (*b*) Three-dimensional merging in a spatially evolving flow, representing a realistic aircraft wake, showing vorticity contours from a large-eddy simulation at $Re = 10^6$. Panel *b* adapted with permission from Laporte (2002).

this process. They were obtained with the same experimental setup as used for the images in **Figure 9*a***, but at a much higher Reynolds number; the evolution is strikingly different. An asymmetry develops in the vortices before merging, and the secondary structures appearing during the later stages of the instability lead to small-scale motion in the final vortex.

Elliptic instability was also observed in the high–Reynolds number simulations of spatially evolving corotating vortices by Laporte (2002) (**Figure 19*b***) and Deniau & Nybelen (2009), representing the wake of an aircraft in a high-lift configuration, with flaps lowered for takeoff or landing. That merging behind each wing occurs much faster than expected from laminar two-dimensional dynamics may partly result from the interference of the shortwave instability. This mechanism is also consistent with earlier experimental observations of unsteadiness (Devenport et al. 1999) and filamentation (Chen et al. 1999) prior to the spatial merging of corotating vortex pairs.

4.2. Combined Crow Instability and Elliptic Instability

In counter-rotating pairs at sufficiently high Reynolds numbers, the Crow and elliptic instabilities develop simultaneously (**Figure 1**). Because the growth rate of the elliptic instability in one vortex scales with the strain induced by the other vortex, and this strain is proportional to b^{-2}, one expects the instability to grow faster in regions where the vortex spacing is reduced. **Figure 1*a*,*b*** clearly shows how the amplitude of the shortwave perturbation is increased at the locations where the Crow instability pushes the vortices toward each other. As for the corotating case, the nonlinear stage of the elliptic instability leads to the inception of secondary structures, which are drawn across to the neighboring vortex, and to a subsequent rapid breakdown into small-scale motion. **Figure 20*a*** shows the resulting turbulent structure, to be compared to the evolution of the pure

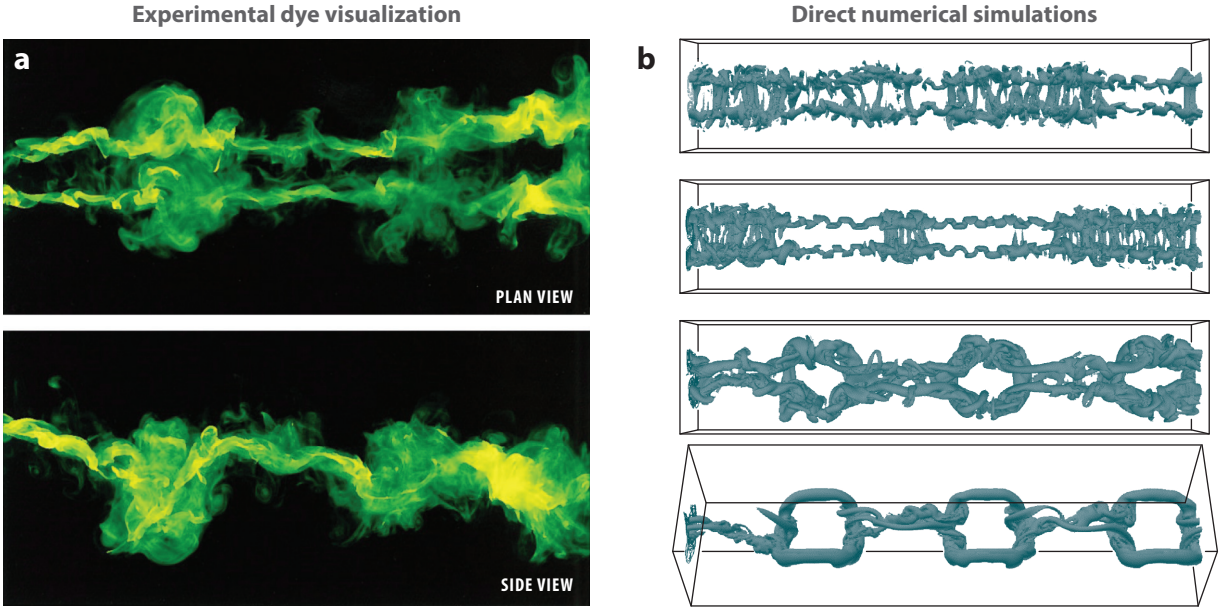

Figure 20

Simultaneous Crow and elliptic instabilities. (*a*) Experimental dye visualization (front and side views) of the late stages after reconnection at $Re = 2{,}750$. Panel *a* adapted with permission from Leweke & Williamson (1998). (*b*) Isosurfaces of the vorticity magnitude from direct numerical simulations at $Re = 2{,}400$, with the instabilities triggered by the addition of random noise. Different cases are shown at the same stage; the ratio of energies initially attributed to the Crow and elliptic instability wave numbers increases from top to bottom. Panel *b* adapted with permission from Laporte & Corjon (2000), copyright AIP Publishing LLC.

Crow instability at lower Reynolds numbers in **Figure 12*a***. One can still distinctly recognize the wavelength of the long-wave Crow instability, which modulates the evolution of the shortwave breakdown.

The precise structure of the late stages of this combined evolution depends on the relative initial amplitude of the respective perturbations. This aspect was explored by Laporte & Corjon (2000), who presented various scenarios, from almost uniform shortwave breakdown to an only slightly perturbed Crow instability, as the initial energy in the Crow mode is increased (**Figure 20*b***).

For high–Reynolds number vortex pairs with significantly smaller core size a/b than those shown in **Figures 1*a*,*b*** and **20*a***, such as realistic aircraft wake vortices, the exchange of fluid via secondary structures will not set in immediately. Each vortex may undergo one or several cycles of shortwave instability-breakdown-relaminarization, mentioned in the previous section, before the Crow instability reduces their separation enough to initiate the exchange. **Figure 1*c*** suggests that, although short waves appear all along the vortices, the violent breakdown observed in laboratory experiments remains localized in the regions of reconnection for these configurations.

5. VORTEX PAIRS NEAR THE GROUND

In this section, we consider the interaction between a vortex pair and a wall or ground surface. Such a configuration is relevant for aircraft near a runway or for junction flows, in which longitudinal vortices are close to a surface. We discuss vortex rebound and the formation of secondary vorticity, coming from the boundary layer between the primary vortices and the ground plane. The secondary vorticity becomes unstable, and we look at the possible sources of the instability, using the stability analyses discussed earlier in this review. In the case of a long-wave instability of the primary vortices interacting with the wall, we find a vortex collapse phenomenon, in which strong axial flows cause distinct topology changes in the vorticity.

The approach of a two-dimensional counter-rotating inviscid point vortex pair to a wall was investigated by Lamb (1932), who showed that the vortices move apart along hyperbolic trajectories. In actual measurements of wing vortex wake data presented by Dee & Nicholas (1968), the vortices appeared to rebound as they approached the surface. This curious effect was successfully explained by Harvey & Perry (1971) and was later studied in simulations by Peace & Riley (1983). As the vortex pair approaches the wall, a boundary layer is formed at the wall beneath each vortex, of opposite-signed vorticity. This boundary layer decelerates in the adverse pressure gradient and ultimately separates from the ground plane, rolling up to form a discrete secondary vortex of opposite sign to the primary one. This induces an upward velocity on the original primary vortex, causing the apparent rebound (see also Orlandi 1990, Kramer et al. 2007). As an illustration of secondary vorticity generation from an essentially two-dimensional flow, **Figure 21** includes a visualization of the interaction between an approaching vortex pair with a horizontal ground plane (Harris & Williamson 2012). Simulations of wing wakes have also been conducted to explore the effects of ambient turbulence, crosswinds, and stratification on a vortex pair near a wall. Many of these cases are discussed in the review by Spalart (1998).

Figure 22*a* displays typical trajectories of the primary vortices, clearly showing the vortex rebound phenomenon. The secondary vortices orbit the primary vortices, as a result of their weaker strength, and the primary vortices are advected away from the wall. We observe a second rebound in **Figure 22*a***, which is associated with the generation of an additional secondary vortex (for multiple rebounds, see Orlandi 1990).

Further characterizing the two-dimensional flow-field development, **Figure 22*b*** presents an example of the time evolution of the circulation. The upper curve represents the slow circulation decay, due to cross-diffusion of vorticity, for an unbounded vortex pair (Asselin & Williamson

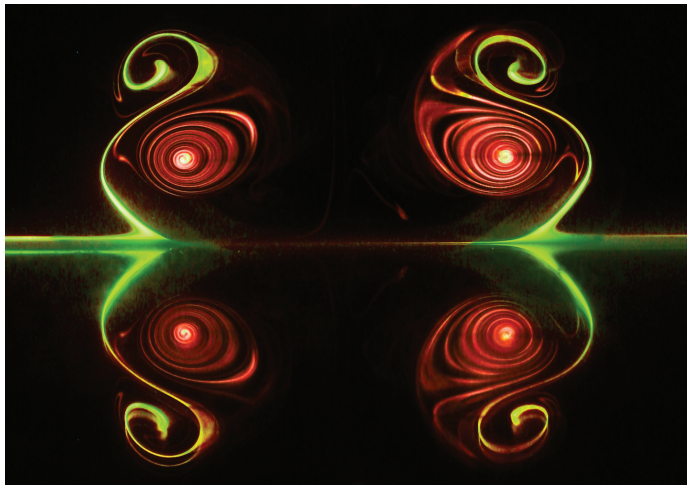

Figure 21

Counter-rotating vortex pair in ground effect. The primary vortices (*red*) descend downward under their self-induced velocity and create a boundary layer at the wall, which can ultimately separate and form secondary vortices (*green*) of opposite rotation. The lower half of the image is a mirror reflection of the vortices in the polished ground plane. Figure reproduced with permission from Harris & Williamson (2012).

2015), which exhibits good agreement with predictions from Cantwell & Rott (1988). In the presence of a ground plane, the primary vortices decay more rapidly in proximity with the secondary vorticity growth near the wall due to diffusion and vorticity cancellation. In essence, vortices in the presence of a wall lose their strength dramatically.

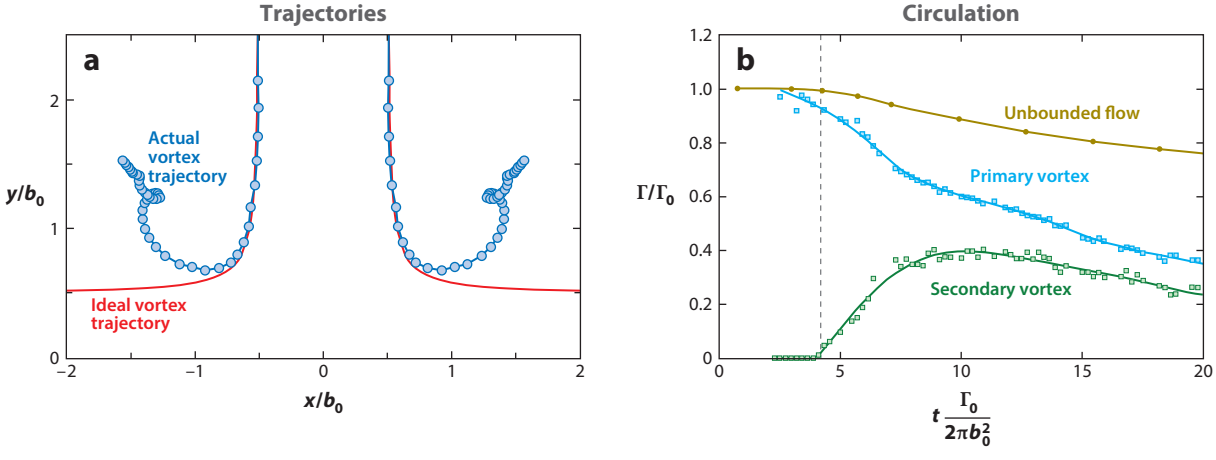

Figure 22

(*a*) Primary vortex trajectories, as measured in experiment, compared with the hyperbolic trajectory of a point vortex pair approaching a horizontal boundary in inviscid flow, as deduced by Lamb (1932). (*b*) Time evolution of circulations of the primary and secondary vortices during two-dimensional ground interaction. Experimental measurements are for $Re = 930$ and an initial height $h_0/b_0 = 5$. Γ_0 and b_0 are the initial circulation and separation distance of the pair, respectively. The dashed line marks the onset of the wall effect.

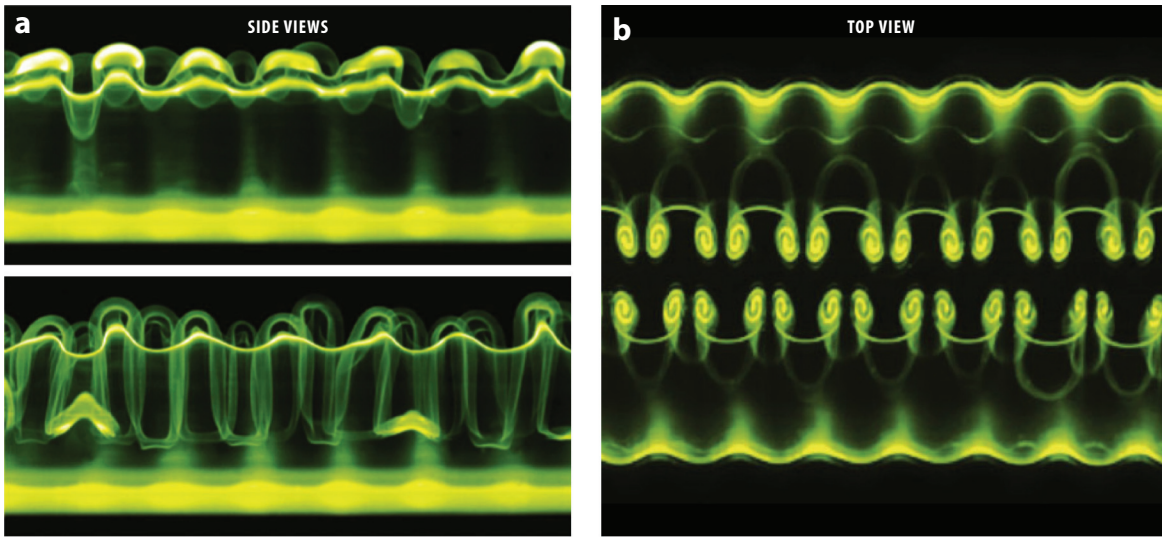

Figure 23

Dye visualization of the three-dimensional Crow-type instability of the secondary vortices at $Re = 1{,}260$. (*a*) Side views, at two different times, with volume illumination. (*b*) Top view, with illumination by a light sheet parallel to the wall placed near the center of the lower image in panel *a*. Figure reproduced with permission from Harris & Williamson (2012).

5.1. Instability of the Secondary Vortex

The secondary vortex develops a waviness, which is shown clearly in the side view of **Figure 23*a***, for $Re = 1{,}260$ (Harris & Williamson 2012). The secondary vortices are between the primary vortices. Because the primary vortices have been kept invisible (only the secondary vortices are selectively marked with fluorescent dye in this case), one may clearly demonstrate an antisymmetric phase relationship between the instabilities of the two secondary vortices. This symmetry is also evident in a horizontal cross-sectional image of the secondary vortex waviness in **Figure 23*b***, where the mushroom vortex pairs move toward each other, ultimately merging the two rows into a single row of alternating-sign vortices. The instability deforms the complete secondary vortex tubes in a displacement mode, rather than an elliptic higher-order radial mode, in which one would observe internal deformations.

The interaction of a single vortex with a wall was originally investigated numerically by Luton & Ragab (1997), who found that the secondary vortex is unstable in the presence of the primary vortex (at $Re = 2{,}196$), inducing what looks like a shortwave displacement bending mode. In the simulations of Duponcheel et al. (2015) at higher Reynolds numbers ($Re = 5{,}200$), there is visual evidence in the early stages (**Figure 24*a***) that the structure of the instability is of an elliptic instability type. In all the above works, the origin of the instability of the weak vortex in a vortex pair was suggested to be of an elliptic-flow type.

To determine the source of such an instability, whether from a Crow-type displacement mode or from an elliptic mode, one must choose for analysis a vortex configuration in which there exists a weaker secondary vortex rotating around a stronger primary vortex (neglecting effects from the other two vortices, as well as from the image vortices). This is quite similar to the four-vortex flow analyzed by Bristol et al. (2004) representing an aircraft wing wake. They recognized that it is essential that the plane containing the perturbation wave rotate with the vortex system, with

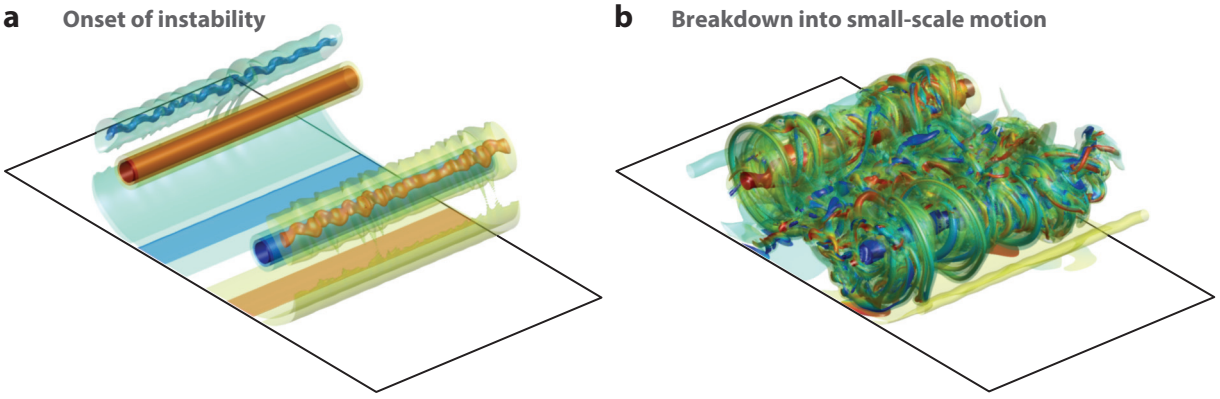

Figure 24

Visualization (by isosurfaces of the vorticity magnitude) of the elliptic instability in the secondary vortices at $Re = 5{,}200$. (*a*) Onset of the instability. (*b*) Breakdown into small-scale motion at later times. Figure reproduced with permission from Duponcheel (2009).

angular velocity Ω (**Figure 2*c***). This significant effect was omitted from the analysis of Luton & Ragab (1997).

The spread of experimental data for the instability wavelength measurements in **Figure 25*a*** is broadly in agreement with the most unstable wavelength for the displacement mode, and is not close to the elliptic mode, according to the inviscid analysis of Harris & Williamson (2012). This inviscid analysis was taken to support the displacement mode observed in the work above and in the simulations of Luton & Ragab (1997). However, Williamson et al. (2014) showed that in the viscous case, the wavelengths of both the most unstable elliptic and displacement modes coincided with experimental measurements; in other words, the wavelength analysis does not decide which

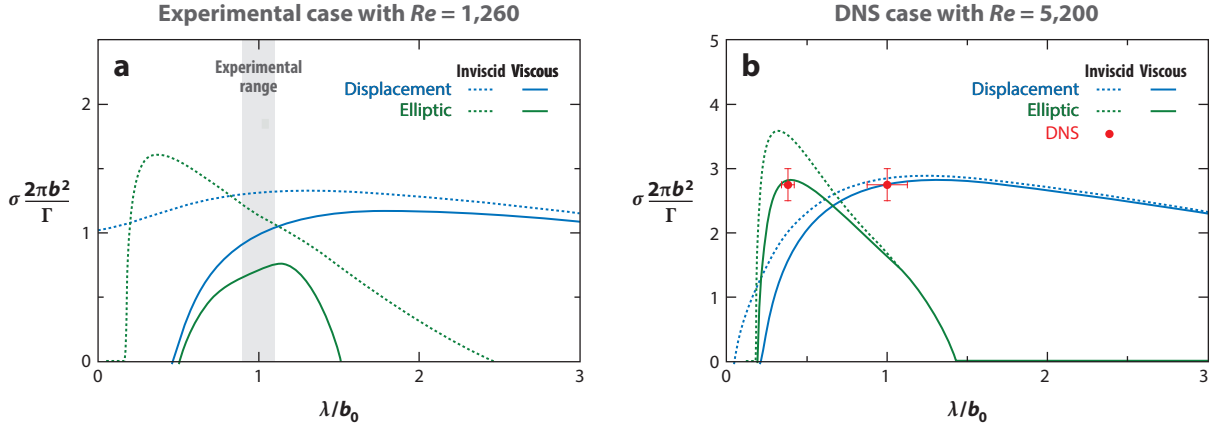

Figure 25

Theoretical predictions of the growth rates of three-dimensional instabilities, based on Equations 8 and 14, for the two cases of vortex pair/ground interactions shown in **Figures 23** and **24**: (*a*) experiment at $Re = 1{,}260$ (Harris & Williamson 2012) and (*b*) direct numerical simulation (DNS) at $Re = 5{,}200$ (M. Duponcheel, C. Cottin, G. Daeninck, G. Winckelmans & T. Leweke, submitted manuscript).

mode is responsible for the instability. However, the growth rate for the displacement mode was greater than that for the elliptic mode, thereby again supporting the observations of the displacement mode in experiments.

A more accurate analysis of the viscous effects in **Figure 25*a***, based on the results in Section 3.2, seems to yield a slightly different conclusion: The larger growth rate of the displacement mode suggests that we would find this mode experimentally. However, the broad range for peak growth rates for this mode (at $Re = 1{,}260$) does not point to a precise instability wavelength. Conversely, the narrower peak of the growth rate curve for the elliptic instability, centered around the experimental range of results, suggests that the length scale is possibly triggered by the elliptic mechanism. Thereafter, the Crow-type displacement mode takes over as the most unstable disturbance, as observed in experiments. At the higher Reynolds number in **Figure 25*b***, M. Duponcheel, C. Cottin, G. Daeninck, G. Winckelmans & T. Leweke (submitted manuscript) found two instability wavelengths in their spatial spectra, which agree remarkably well with the peak growth rates of the elliptic instability and of the displacement mode. In the simulations, the elliptic instability (**Figure 24*a***) is clearly evident initially at the wavelength $\lambda/b_0 = 0.4$, followed by spectral evidence of the displacement mode, $\lambda/b_0 = 1.0$. As the Reynolds number increases, the most unstable wavelengths for the two modes become distinctly different.

5.2. Crow Instability in Ground Effect

We here briefly discuss some essential characteristics of the influence of ground proximity on the development of long-wave instability. (The initial instability is described in Section 3.1.) It is clear that if the initial height of the vortex pair above the surface is large, then the Crow instability, and the eventual redistribution of vorticity into vortex rings, will occur prior to wall interaction. Correspondingly, one must also expect that, if the vortex pair is generated below a critical height to the surface, then there will not be enough time for the long-wave instability to take hold before the vortices are separated from each other in wall effect; one might expect that the long-wavelength instability will be inhibited.

In essence, three regimes of vortex-surface interaction are found, depending on the initial height at which the vortex pairs are generated (Asselin & Williamson 2015). Each regime involves the phenomenon of vortex collapse by which strong local axial flows develop, and a segment of the original vortex tube is reduced to a concentrated region of vorticity, often leaving behind very thin wisps of dye marking weak vorticity. A feature of these flows is that small vortex rings are generated from the concentrated regions. An example of this phenomenon is seen in **Figure 26** for moderate initial height. The resulting structure is remarkably similar to the small-scale structure that is left behind when a vortex ring impinges upon a wall obliquely (Lim 1989). The pressure-driven axial flows transport vorticity away from the parts of the vortex that first come in contact with the ground plane. This is as true for the ring as it is for the vortex segments found in **Figure 26**.

Measurements of the instability amplitude also clearly show the effects of the wall proximity (**Figure 27**). The amplitude growth of the waviness is inhibited by the presence of the ground, and the rather sudden stop to the amplitude increase is correlated with the growth of secondary vorticity, along with a reduction in the strength of the primary vortex (see the curve for height $b_0/b_0 = 5$). For the larger initial height ($b_0/b_0 = 10$), the classical vortex rings are formed before interacting with the ground, but again the growth of amplitude is diminished as the vortices encounter secondary vorticity at the wall.

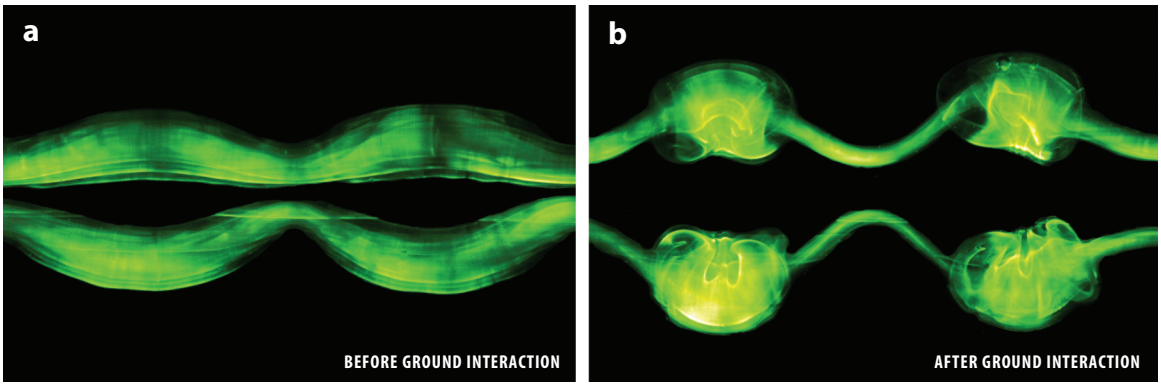

Figure 26

Dye visualization of the development of the Crow instability in the presence of a wall, for a moderate initial height of the pair ($b_0/b_0 = 7.5$). Primary vortices viewed from below (*a*) before significant ground interaction and (*b*) after ground interaction, when strong local axial flows have generated the set of concentrated vortices (which turn out to be small vortex rings). Figure reproduced with permission from Asselin & Williamson (2013), copyright AIP Publishing LLC.

In summary, the principal characteristics of the long-wave instability in the presence of the wall are as follows:

- Even a very slight waviness in each vortex, as it approaches the wall, can trigger a large pressure gradient and axial flow that strips away the vortex filaments at the trough and forms concentrated vortices at the peak. One might conclude that the effect of a surface interacting

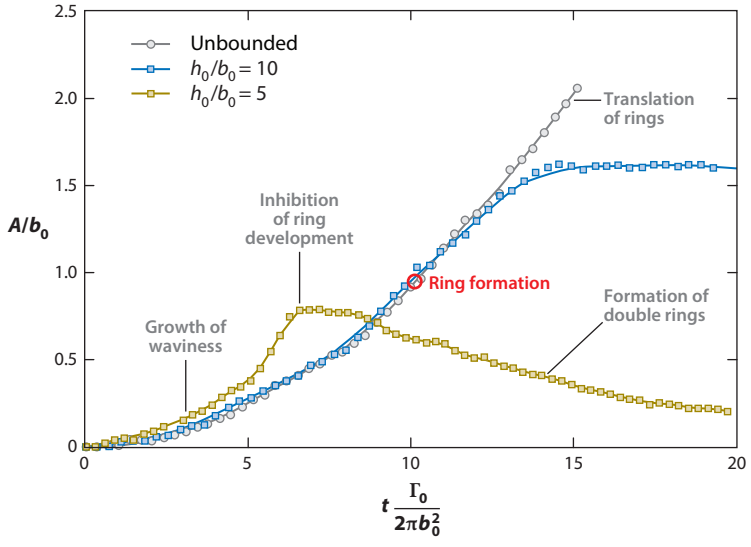

Figure 27

Growth of the Crow instability amplitude A (defined in **Figure 13*a***), as a function of the initial distance b_0 from the wall at $Re \approx 1{,}000$. For the closest distance, the reconnection and ring formation are completely inhibited by the interaction with the wall. Figure adapted with permission from Asselin & Williamson (2015).

with a small perturbation on an otherwise parallel vortex is enough to cause surprisingly large three-dimensional effects. This might be seen as a fundamental characteristic for a vortex aligned with a surface.

- The concentrated vortices at the peak either evolve into vertical vortex rings of large diameter or into smaller horizontal vortex rings, which rise up away from the wall. In essence, vortex rings are ubiquitous in these flows, despite the apparent complexity of the vortex interactions.
- The Crow instability is inhibited by the presence of the ground, if the initial vortex pair height is below a critical value.

Finally, it is interesting to note that a single vortex parallel to a solid surface can also be subject to both Crow and elliptic instabilities, by effectively forming a counter-rotating pair with its image. This feature was analyzed by Rabinovitch et al. (2012) and Benton & Bons (2014) in the context of blade tip leakage in turbomachinery.

6. CONCLUDING REMARKS

In this review, we discuss the physical mechanisms involved in the dynamics of pairs of parallel vortices. We have restricted ourselves to cases in which each vortex retains its identity long enough to develop the various phenomena (instabilities). This excludes certain combinations of circulations and core sizes, for which transient dynamics result in a rapid alteration or destruction of one of the vortices (**Figure 11**). This conceptually simple flow can be investigated in detail by theoretical, experimental, and numerical techniques, and several new results have been obtained over the past three decades. They show in general very good agreement; examples of direct comparisons of different approaches can be found in Leweke et al. (2001), Laporte & Leweke (2002), and Le Dizès & Laporte (2002).

We have focused on the mechanisms causing the initial transformation of a given vortex pair. The later evolution of the flow involves other fundamental flow phenomena, such as vortex reconnection (Kida & Takaoka 1994) or vortex ring dynamics (Shariff & Leonard 1992) for the case of the Crow instability. They are not considered further here; they deserve a (new) review of their own. Additional effects such as fluid stratification (see the sidebar, Vortex Pairs in a Stratified Fluid), external turbulence (Holzäpfel et al. 2003), and background rotation (Hopfinger & van Heijst 1993, van Heijst & Clercx 2009), which have relevance for aeronautical and geophysical applications, are also beyond the scope of this review.

SUMMARY POINTS

1. Two parallel vortices in a homogeneous fluid either translate or rotate around each other, without changing their separation distance. The strain induced by one vortex in its neighborhood is enhanced inside the core of the second vortex by the nonlinear interaction with the vorticity. This effect depends on the rotation of the system.
2. Merging of a corotating pair arises when the core sizes are increased beyond a critical fraction of the separation distance by viscous diffusion. Several dissipative and convective stages can be identified. Rapid convective merging can be understood by considering the vorticity dynamics in the streamline pattern of the corotating reference frame. It generates antisymmetric vorticity, which causes merging.

3. Counter-rotating pairs are unstable with respect to three-dimensional displacement perturbations (Crow instability). This results from the combination of mutually and self-induced dynamics of the vortices, involving rotation and straining of the wavy perturbations. Unstable axial wavelengths are in the range of 5–10 vortex spacings for equal-strength pairs but can be as low as one spacing for unequal vortices. The former evolve into a series of vortex rings through a reconnection process, whereas in the latter the weaker vortex is deformed into periodic loops.
4. For sufficiently high Reynolds numbers, all pairs are subject to shortwave instabilities of the vortex cores. These are induced by a resonance between the mutually induced strain, which makes the core streamlines elliptic, and linear Kelvin modes of the vortex. The characteristic unstable perturbations of this elliptic instability have wavelengths of the order of the core diameter. Their structure varies in the presence of axial flow inside the vortices. The nonlinear evolution of the elliptic instability leads to a breakdown into small-scale turbulent motion and rapid dissipation.
5. Elliptic instability can interfere with other phenomena. It can lead to the premature merging of corotating pairs, with a larger and more turbulent final vortex, or to the breakdown of a counter-rotating pair, in combination with the Crow instability.
6. The mode structures of the three-dimensional instabilities, and complete sets of equations for the determination of the respective growth rates in pairs of arbitrary unequal vortices, can be used to identify these phenomena in other situations involving the interaction of parallel or nearly parallel vortices.
7. One such configuration is the descending vortex pair in ground effect, in which secondary vortices are formed from the boundary layer separating from the wall, leading to the rebound of the pair. These vortices form unequal pairs with the primary vortices, which can exhibit both Crow and elliptic instabilities. Different evolutions can be predicted from theory, depending primarily on the Reynolds number, in good agreement with observations.

FUTURE ISSUES

1. The basic mechanism for vortex merging now seems well established, but some open questions remain, in particular concerning high Reynolds numbers. The precise origin of the transition (transient evolution versus instability) is also still under debate.
2. The analysis of long-wave interactions of vortex filaments can be extended to more complex configurations, also involving an initial curvature and torsion of the vortices. Examples are arrays of vortex rings and helical vortices, which have previously been studied by Levy & Forsdyke (1927) and Widnall (1972). Helical vortex systems have recently regained interest in the context of rotor wake aerodynamics (Vermeer et al. 2003, Leishman 2006, Felli et al. 2011).
3. Curvature and torsion also have an effect on the shortwave core instabilities. The Kelvin-mode coupling induced by curvature is different from the one caused by an external strain. Fukumoto & Hattori (2005) have predicted a shortwave curvature instability for

Rankine-type vortices. Current research is concerned with an extension of these results to vortices with smooth vorticity profiles (also including axial flow) and with a first experimental or numerical observation of this instability.

DISCLOSURE STATEMENT

The authors are not aware of any biases that might be perceived as affecting the objectivity of this review.

ACKNOWLEDGMENTS

The authors thank Paolo Luzzatto-Fegiz, Dan Harris, and Dan Asselin for their help with the preparation of this review. T.L. and S.L.D. acknowledge financial support from the French Agence Nationale de la Recherche (contract ANR-05-BLAN-0241 "Vortex") and from the European Commission (contract AST4-CT-2005-012238 "FAR-Wake"). C.H.K.W. gratefully acknowledges the support from the US Office of Naval Research, monitored by Dr. Ron Joslin, under award number N00014-12-1-0712.

LITERATURE CITED

Asselin DJ, Williamson CHK. 2013. Vortex pair impinging on a horizontal ground plane. *Phys. Fluids* 25:091104

Asselin DJ, Williamson CHK. 2015. Influence of a ground plane on the long-wave three-dimensional instability of a vortex. *J. Fluid Mech.* Submitted manuscript

Batchelor GK. 1964. Axial flow in trailing line vortices. *J. Fluid Mech.* 20:645–58

Bayly BJ. 1986. Three-dimensional instability of elliptical flow. *Phys. Rev. Lett.* 57:2160–63

Benton SI, Bons JP. 2014. *Three-dimensional instabilities in vortex/wall interactions: linear stability and flow control.* Presented at Aerosp. Sci. Meet., 52nd, National Harbor, MD, AIAA Pap. 2014-1267

Billant P. 2010. Zigzag instability of vortex pairs in stratified and rotating fluids. Part 1. General stability equations. *J. Fluid Mech.* 660:354–95

Billant P, Brancher P, Chomaz JM. 1999. Three-dimensional stability of a vortex pair. *Phys. Fluids* 11:2069–77

Billant P, Chomaz JM. 2000. Experimental evidence for a new instability of a vertical columnar vortex pair in a strongly stratified fluid. *J. Fluid Mech.* 418:167–88

Brandt LK, Nomura KK. 2007. The physics of vortex merger and the effects of ambient stable stratification. *J. Fluid Mech.* 592:413–46

Brandt LK, Nomura KK. 2010. Characterization of interactions of two unequal co-rotating vortices. *J. Fluid Mech.* 646:233–53

Breitsamter C. 2011. Wake vortex characteristics of transport aircraft. *Progr. Aerosp. Sci.* 47:89–134

Brion V, Sipp D, Jacquin L. 2014. Linear dynamics of the Lamb-Chaplygin dipole in the two-dimensional limit. *Phys. Fluids* 26:064103

Bristol RL, Ortega JM, Marcus PS, Savaş O. 2004. On cooperative instabilities of parallel vortex pairs. *J. Fluid Mech.* 517:331–58

Cantwell B, Rott N. 1988. The decay of a viscous vortex pair. *Phys. Fluids* 31:3213–24

Cerretelli C, Williamson CHK. 2003a. A new family of uniform vortices related to vortex configurations before merging. *J. Fluid Mech.* 493:219–29

Cerretelli C, Williamson CHK. 2003b. The physical mechanism for vortex merging. *J. Fluid Mech.* 475:41–77

Chatelain P, Curioni A, Bergdorf M, Rossinelli D, Andreoni W, Koumoutsakos P. 2008. Billion vortex particle direct numerical simulations of aircraft wakes. *Comput. Methods Appl. Mech. Eng.* 197:1296–304

Chen AL, Jacob JD, Savaş O. 1999. Dynamics of corotating vortex pairs in the wakes of flapped airfoils. *J. Fluid Mech.* 382:155–93

Crouch J, Jacquin L, eds. 2005. Aircraft trailing vortices/Tourbillons de sillages d'avions. *C. R. Phys.* 6(4–5, Spec. Issue). Amsterdam: Elsevier

Studies four-vortex configurations for rapid aircraft wake breakup.

Crouch JD, Miller GD, Spalart PR. 2001. Active-control system for breakup of airplane trailing vortices. *AIAA J.* 39:2374–81

Provides a theoretical description of the long-wave displacement instability of counter-rotating vortices.

Crow SC. 1970. Stability theory for a pair of trailing vortices. *AIAA J.* 8:2172–79

Dee FW, Nicholas OP. 1968. *Flight measurements of wing-tip vortex motion near the ground*. Tech. Rep. CP 1065, Br. Aeronaut. Res. Council

Delisi DP, Robins RE. 2000. Short-scale instabilities in trailing wake vortices in a stratified fluid. *AIAA J.* 38:1916–23

Deniau H, Nybelen L. 2009. Strategy for spatial simulation of co-rotating vortices. *Int. J. Numer. Methods Fluids* 61:23–56

Devenport WJ, Vogel CM, Zsoldos JS. 1999. Flow structure produced by the interaction and merger of a pair of co-rotating wing-tip vortices. *J. Fluid Mech.* 394:357–77

Dhanak MR, De Bernardinis B. 1981. The evolution of an elliptic vortex ring. *J. Fluid Mech.* 109:189–216

Donnadieu C, Ortiz S, Chomaz JM, Billant P. 2009. Three-dimensional instabilities and transient growth of a counter-rotating vortex pair. *Phys. Fluids* 21:094102

Presents the first linear stability analysis of uniform corotating, equal-area vortex pairs.

Dritschel DG. 1985. The stability and energetics of corotating uniform vortices. *J. Fluid Mech.* 157:95–134

Dritschel DG. 1986. The nonlinear evolution of rotating configurations of uniform vorticity. *J. Fluid Mech.* 172:157–82

Dritschel DG. 1995. A general theory for two-dimensional vortex interactions. *J. Fluid Mech.* 293:269–303

Dritschel DG, Waugh DW. 1992. Quantification of the inelastic interaction of unequal vortices in two-dimensional vortex dynamics. *Phys. Fluids A* 4:1737–44

Duponcheel M. 2009. *Direct and large-eddy simulation of turbulent wall-bounded flows*. PhD Thesis, Univ. Cathol. Louvain

Ehrenstein U, Rossi M. 1999. Equilibria of corotating nonuniform vortices. *Phys. Fluids* 25:3416–25

Eloy C, Le Dizès S. 1999. Three-dimensional instability of Burgers and Lamb-Oseen vortices in a strain field. *J. Fluid Mech.* 378:145–66

Eloy C, Le Dizès S. 2001. Stability of the Rankine vortex in a multipolar strain field. *Phys. Fluids* 13:660–76

Eloy C, Le Gal P, Le Dizès S. 2003. Elliptic and triangular instabilities in rotating cylinders. *J. Fluid Mech.* 476:357–88

Fabre D. 2002. *Instabilitités et instationnarités dans les tourbillons: application aux sillages d'avions*. PhD Thesis, Univ. Paris VI

Fabre D, Jacquin L, Loof A. 2002. Optimal perturbations in a four-vortex aircraft wake in counter-rotating configuration. *J. Fluid Mech.* 451:319–28

Fabre D, Sipp D, Jacquin L. 2006. The Kelvin waves and the singular modes of the Lamb-Oseen vortex. *J. Fluid Mech.* 551:235–74

Felli M, Camussi R, Felice FD. 2011. Mechanisms of evolution of the propeller wake in the transition and far fields. *J. Fluid Mech.* 682:5–53

Fukumoto Y. 2003. The three-dimensional instability of a strained vortex tube revisited. *J. Fluid Mech.* 493: 287–318

Fukumoto Y, Hattori Y. 2005. Curvature instability of a vortex ring. *J. Fluid Mech.* 526:77–115

Garten JF, Werne J, Fritts DC, Arendt S. 2001. Direct numerical simulations of the Crow instability and subsequent vortex reconnection in a stratified fluid. *J. Fluid Mech.* 426:1–45

Gerz T, Holzäpfel F, Darracq D. 2002. Commercial aircraft wake vortices. *Progr. Aerosp. Sci.* 38:181–208

Harris DM, Williamson CHK. 2012. Instability of secondary vortices generated by a vortex pair in ground effect. *J. Fluid Mech.* 700:148–86

Harvey JK, Perry FJ. 1971. Flowfield produced by trailing vortices in the vicinity of the ground. *AIAA J.* 9:1659–60

Holzäpfel F, Gerz T, Baumann R. 2001. The turbulent decay of trailing vortex pairs in stably stratified environments. *Aerosp. Sci. Technol.* 5:95–108

Holzäpfel F, Hofbauer T, Darracq D, Moet H, Garnier F, Ferreira Gago C. 2003. Analysis of wake vortex decay mechanisms in the atmosphere. *Aerosp. Sci. Technol.* 7:263–75
Hopfinger EJ, van Heijst GJF. 1993. Vortices in rotating fluids. *Annu. Rev. Fluid Mech.* 25:241–89
Jiménez J. 1975. Stability of a pair of co-rotating vortices. *Phys. Fluids* 18:1580–81
Jing F, Kanso E, Newton PK. 2012. Insights into symmetric and asymmetric vortex mergers using the core growth model. *Phys. Fluids* 24:073101
Josserand C, Rossi M. 2007. The merging of two co-rotating vortices: a numerical study. *Eur. J. Mech. B Fluids* 26:779–94
Kelvin L. 1880. On the vibrations of a columnar vortex. *Philos. Mag.* 10:155–68
Kerswell RR. 1999. Secondary instabilities in rapidly rotating fluids: inertial wave breakdown. *J. Fluid Mech.* 382:283–306
Kerswell RR. 2002. Elliptical instability. *Annu. Rev. Fluid Mech.* 34:83–113
Kida S, Takaoka M. 1994. Vortex reconnection. *Annu. Rev. Fluid Mech.* 26:169–77
Klein R, Majda AJ, Damodaran K. 1995. Simplified equations for the interaction of nearly parallel vortex filaments. *J. Fluid Mech.* 288:201–48
Kramer W, Clercx HJH, van Heijst GJF. 2007. Vorticity dynamics of a dipole colliding with a no-slip wall. *Phys. Fluids* 19:126603
Lacaze L, Birbaud AL, Le Dizès S. 2005. Elliptic instability in a Rankine vortex with axial flow. *Phys. Fluids* 17:017101
Lacaze L, Ryan K, Le Dizès S. 2007. Elliptic instability in a strained Batchelor vortex. *J. Fluid Mech.* 577:341–61
Lamb H. 1932. *Hydrodynamics.* Cambridge, UK: Cambridge Univ. Press. 6th ed.
Landman MJ, Saffman PG. 1987. The three-dimensional instability of strained vortices in a viscous fluid. *Phys. Fluids* 30:2339–42
Laporte F. 2002. *Simulation numérique appliquée à la caractérisation et aux instabilités des tourbillons de sillage des avions de transport*. PhD Thesis, INPT, Toulouse
Laporte F, Corjon A. 2000. Direct numerical simulations of the elliptic instability of a vortex pair. *Phys. Fluids* 12:1016–31
Laporte F, Leweke T. 2002. Elliptic instability of trailing vortices: experiment and direct numerical simulation. *AIAA J.* 40:2483–94
Le Dizès S. 2000a. Non-axisymmetric vortices in two-dimensional flows. *J. Fluid Mech.* 406:175–98
Le Dizès S. 2000b. Three-dimensional instability of a multipolar vortex in a rotating flow. *Phys. Fluids* 12:2762–74
Le Dizès S. 2004. Viscous critical-layer analysis of vortex normal modes. *Stud. Appl. Math.* 112:315–32
Le Dizès S, Lacaze L. 2005. An asymptotic description of vortex Kelvin modes. *J. Fluid Mech.* 542:69–96
Le Dizès S, Laporte F. 2002. Theoretical predictions for the elliptic instability in a two-vortex flow. *J. Fluid Mech.* 471:169–201
Le Dizès S, Verga A. 2002. Viscous interaction of two co-rotating vortices before merging. *J. Fluid Mech.* 467:389–410
Legras B, Dritschel DG. 1993. Vortex stripping and the generation of high vorticity gradients in two-dimensional flows. *Appl. Sci. Res.* 51:445–55
Leishman JG. 2006. *Principles of Helicopter Aerodynamics.* Cambridge, UK: Cambridge Univ. Press
Levy H, Forsdyke AG. 1927. The stability of an infinite system of circular vortices. *Proc. R. Soc. Lond. A* 114:594–604
Leweke T, Meunier P, Laporte F, Darracq D. 2001. *Controlled interaction of co-rotating vortices*. Presented at 3rd ONERA-DLR Aerosp. Symp. (ODAS 2001), Paris, Pap. S2-3
Leweke T, Williamson CHK. 1998. Cooperative elliptic instability of a vortex pair. *J. Fluid Mech.* 360:85–119
Leweke T, Williamson CHK. 2011. Experiments on long-wavelength instability and reconnection of a vortex pair. *Phys. Fluids* 23:024101
Lim TT. 1989. An experimental study of a vortex ring interacting with an inclined wall. *Exp. Fluids* 7:453–63
Luton JA, Ragab SA. 1997. The three-dimensional interaction of a vortex pair with a wall. *Phys. Fluids* 9:2967–80

Describes the effect of axial flow on elliptic instability in realistic vortices.

Presents a general formula for the elliptic instability growth rate in a vortex pair.

Provides the first experimental identification of the elliptic instability in an open flow.

Luzzatto-Fegiz P, Williamson CHK. 2010. Stability of elliptical vortices from "Imperfect-Velocity-Impulse" diagrams. *Theor. Comput. Fluid Dyn.* 24:181–88
Luzzatto-Fegiz P, Williamson CHK. 2012. Determining the stability of steady two-dimensional flows through imperfect velocity-impulse diagrams. *J. Fluid Mech.* 706:323–50
Mariotti A, Legras B, Dritschel DG. 1994. Vortex stripping and the erosion of coherent structures in two-dimensional flows. *Phys. Fluids A* 6:3954–62
Mayer EW, Powell KG. 1992. Viscous and inviscid instabilities of a trailing vortex. *J. Fluid Mech.* 245:91–114
Melander MV, McWilliams JC, Zabusky NJ. 1987. Axisymmetrization and vorticity-gradient intensification of an isolated two-dimensional vortex through filamentation. *J. Fluid Mech.* 178:137–59
Melander MV, Zabusky NJ, McWilliams JC. 1988. Symmetric vortex merger in two-dimensions: causes and conditions. *J. Fluid Mech.* 195:303–40
Meunier P, Ehrenstein U, Leweke T, Rossi M. 2002. A merging criterion for two-dimensional co-rotating vortices. *Phys. Fluids* 14:2757–66
Meunier P, Le Dizès S, Leweke T. 2005. Physics of vortex merging. *C. R. Phys.* 6:431–50
Meunier P, Leweke T. 2000. Unstable vortex merger. *Phys. Fluids* 12:S6

Presents experimental observations of elliptic instability in corotating vortices.

Meunier P, Leweke T. 2001. Three-dimensional instability during vortex merging. *Phys. Fluids* 13:2747–50

Meunier P, Leweke T. 2005. Elliptic instability of a co-rotating vortex pair. *J. Fluid Mech.* 533:125–59
Miyazaki T, Fukumoto Y. 1992. Three-dimensional instability of strained vortices in stably stratified fluid. *Phys. Fluids A* 4:2515–22
Moffatt HK, Kida S, Ohkitani K. 1994. Stretched vortices: the sinews of turbulence; large-Reynolds-number asymptotics. *J. Fluid Mech.* 259:241–64
Moore DW, Saffman PG. 1971. Structure of a line vortex in an imposed strain. In *Aircraft Wake Turbulence and Its Detection*, ed. JH Olsen, A Goldburg, M Rogers, pp. 339–54. New York: Plenum

Explains how elliptic instability is associated with a mechanism of Kelvin-mode resonance.

Moore DW, Saffman PG. 1975. The instability of a straight vortex filament in a strain field. *Proc. R. Soc. Lond. A* 346:413–25

NATO (N. Atl. Treaty Organ.), ed. 1996. *The Characterization and Modification of Wakes from Lifting Vehicles in Fluids*. Vol. 584 NATO AGARD Conf. Proc. Brussels: NATO
Nomura KK, Tsutsui H, Mahoney D, Rottman JW. 2006. Short-wavelength instability and decay of a vortex pair in a stratified fluid. *J. Fluid Mech.* 553:283–322
Nybelen L, Paoli R. 2009. Direct and large-eddy simulations of merging in corotating vortex system. *AIAA J.* 47:157–67
Orlandi P. 1990. Vortex dipole rebound from a wall. *Phys. Fluids A* 2:1429–36
Ortega JM, Bristol RL, Savaş O. 2003. Experimental study of the instability of unequal-strength counter-rotating vortex pairs. *J. Fluid Mech.* 474:35–84
Otheguy P, Billant P, Chomaz JM. 2006. The effect of planetary rotation on the zigzg instability of co-rotating vortices in a stratified fluid. *J. Fluid Mech.* 553:273–81
Otheguy P, Chomaz JM, Augier P, Kimura Y, Billant P. 2015. Pairing of two vertical columnar vortices in a stratified fluid. *Eur. J. Mech. B Fluids* 49:413–25
Overman EA, Zabusky NJ. 1982. Evolution and merger of isolated vortex structures. *Phys. Fluids* 25:1297–305
Peace AJ, Riley N. 1983. A viscous vortex pair in ground effect. *J. Fluid Mech.* 129:409–26
Pierrehumbert RT. 1986. Universal short-wave instability of two-dimensional eddies in an inviscid fluid. *Phys. Rev. Lett.* 57:2157–60
Pullin DI. 1992. Contour dynamics methods. *Annu. Rev. Fluid Mech.* 24:89–115
Rabinovitch J, Brion V, Blanquart G. 2012. Effect of a splitter plate on the dynamics of a vortex pair. *Phys. Fluids* 24:074110
Roberts KV, Christiansen JP. 1972. Topics in computational fluid mechanics. *Comput. Phys. Commun. Suppl.* 3:14–32
Rossow VJ. 1999. Lift-generated vortex wakes of subsonic transport aircraft. *Prog. Aerosp. Sci.* 35:507–660
Roy C, Leweke T, Thompson MC, Hourigan K. 2011. Experiments on the elliptic instability in vortex pairs with axial core flow. *J. Fluid Mech.* 677:383–416
Roy C, Schaeffer N, Le Dizès S, Thompson M. 2008. Stability of a pair of co-rotating vortices with axial flow. *Phys. Fluids* 20:094101

Ryan K, Butler CJ, Sheard GJ. 2012. Stability characteristics of a counter-rotating unequal-strength Batchelor vortex pair. *J. Fluid Mech.* 696:374–401
Ryan K, Sheard GJ. 2007. Non-linear growth of short-wave instabilities in a Batchelor vortex pair. *Proc. 16th Australas. Fluid Mech. Conf.*, ed. P Jacobs, T McIntyre, M Cleary, D Buttsworth, D Mee, et al. pp. 1463–69. Brisbane: Univ. Queensland
Saffman PG. 1992. *Vortex Dynamics*. Cambridge, UK: Cambridge Univ. Press
Saffman PG, Szeto R. 1980. Equilibrium of a pair of equal uniform vortices. *Phys. Fluids* 23:2339–42
Schaeffer N, Le Dizès S. 2007. Influence of an elliptic instability on the merging of a co-rotating vortex pair. In *18ème Congrès Français de Mécanique*, Pap. CFM2007-1038. Courbevoie: AFM
Schaeffer N, Le Dizès S. 2010. Nonlinear dynamics of the elliptic instability. *J. Fluid Mech.* 646:471–80
Shariff K, Leonard A. 1992. Vortex rings. *Annu. Rev. Fluid Mech.* 24:235–79
Sipp D, Jacquin L. 2003. Widnall instabilities in vortex pairs. *Phys. Fluids* 15:1861–74
Sipp D, Jacquin L, Cossu C. 2000. Self-adaptation and viscous selection in concentrated two-dimensional dipoles. *Phys. Fluids* 12:245–48
So J, Ryan K, Sheard GS. 2011. Short-wave instabilities on a vortex pair of unequal strength circulation ratio. *Appl. Math. Model.* 35:1571–90
Spalart PR. 1998. Airplane trailing vortices. *Annu. Rev. Fluid Mech.* 30:107–38
Ting L, Tung C. 1965. Motion and decay of a vortex in a nonuniform stream. *Phys. Fluids* 8:1039–51
Trieling RR, Beckers M, van Heijst GJF. 1997. Dynamics of monopolar vortices in a strain flow. *J. Fluid Mech.* 345:165–201
Trieling RR, Velasco Fuentes OU, van Heijst GJF. 2005. Interaction of two unequal corotating vortices. *Phys. Fluids* 17:087103
Tsai CY, Widnall SE. 1976. The stability of short waves on a straight vortex filament in a weak externally imposed strain field. *J. Fluid Mech.* 73:721–33
van Heijst GJF, Clercx HJH. 2009. Laboratory modeling of geophysical vortices. *Annu. Rev. Fluid Mech.* 41:143–64
Velasco Fuentes OU. 2005. Vortex filamentation: its onset and its role on axisymmetrization and merger. *Dyn. Atmos. Oceans* 40:23–42
Vermeer LJ, Sørensen JN, Crespo A. 2003. Wind turbine wake aerodynamics. *Progr. Aerosp. Sci.* 39:467–510
Waite ML, Smolarkiewicz. 2008. Instability and breakdown of a vertical vortex pair in a strongly stratified fluid. *J. Fluid Mech.* 606:239–73
Waleffe F. 1989. *The 3D instability of a strained vortex and its relation to turbulence*. PhD Thesis, Mass. Inst. Technol., Cambridge
Waleffe F. 1990. On the three-dimensional instability of strained vortices. *Phys. Fluids A* 2:76–80
Widnall SE. 1972. The stability of a helical vortex filament. *J. Fluid Mech.* 54:641–63
Widnall SE. 1975. The structure and dynamics of vortex filaments. *Annu. Rev. Fluid Mech.* 7:141–65
Widnall SE, Bliss D, Tsai CY. 1974. The instability of short waves on a vortex ring. *J. Fluid Mech.* 66:35–47
Widnall SE, Bliss DB, Zalay A. 1971. Theoretical and experimental study of the instability of a vortex pair. In *Aircraft Wake Turbulence and Its Detection*, ed. JH Olsen, A Goldburg, M Rogers, pp. 305–38. New York: Plenum
Williamson CHK, Chomaz JM. 1997. The exploding vortex pair. *Phys. Fluids* 9:S4
Williamson CHK, Leweke T, Asselin DJ, Harris DM. 2014. Phenomena, dynamics and instabilities of vortex pairs. *Fluid Dyn. Res.* 46:061425
Winckelmans G, Cocle R, Dufresne L, Capart R. 2005. Vortex methods and their application to trailing wake vortex simulations. *C. R. Phys.* 6:467–86
Yasuda I, Flierl GR. 1995. Two-dimensional asymmetric vortex merger: contour dynamics experiment. *J. Oceanogr.* 51:145–70

Provides the link between local and global descriptions of the elliptic instability.

Presents the first theoretical description of the elliptic instability.

Annual Review of
Fluid Mechanics

Volume 48, 2016

Contents

Indexes

Errata

An online log of corrections to *Annual Review of Fluid Mechanics* articles may be found at http://www.annualreviews.org/errata/fluid